

AD-A110 396

MINNESOTA UNIV MINNEAPOLIS DEPT OF MECHANICAL ENGIN--ETC F/6 20/13
STUDIES OF HEAT TRANSFER IN COMPLEX INTERNAL FLOWS.(U)

JAN 82 E M SPARROW, S V PATANKAR

N00014-79-C-0621

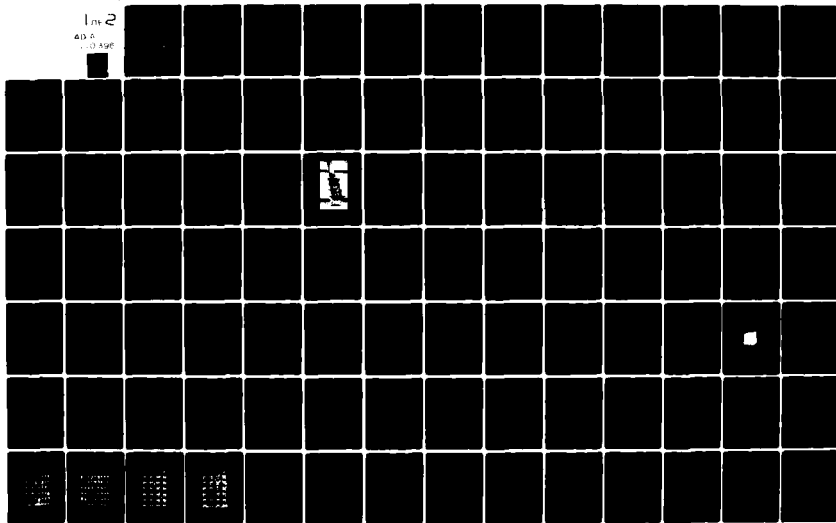
UNCLASSIFIED

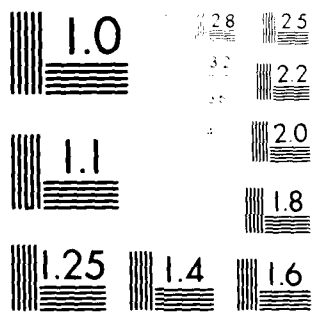
NL

1 of 2

AD-A

0-196





MEGACOLOR RESOLUTION TEST CHART
NO. 1010 100% ISO

(12)

LEVEL

AD A110396

STUDIES OF HEAT TRANSFER IN COMPLEX INTERNAL FLOWS

E. M. Sparrow

S. V. Patankar

Second Summary Report
Contract N00014-79-C-0621
Office of Naval Research

January, 1982

DTIC
ELECTE
S FEB 2 1982 D
B

Department of Mechanical Engineering
University of Minnesota
Minneapolis, Minnesota 55455

DISTRIBUTION STATEMENT A

Approved for public release
Distribution Unlimited

DTIC FILE COPY

82 02 01 015

REPORT DOCUMENTATION PAGE		READ INSTRUCTIONS BEFORE COMPLETING FORM
1. REPORT NUMBER N00014-79-C-0621-1982A	2. GOVT ACCESSION NO. AD A110 316	3. RECIPIENT'S CATALOG NUMBER
4. TITLE (and Subtitle) STUDIES OF HEAT TRANSFER IN COMPLEX INTERNAL FLOWS		5. TYPE OF REPORT & PERIOD COVERED Summary Report Dec.15,1980 to Dec.15,1981
		6. PERFORMING ORG. REPORT NUMBER
7. AUTHOR(s) E. M. Sparrow and S. V. Patankar		8. CONTRACT OR GRANT NUMBER(s) N00014-79-C-0621
9. PERFORMING ORGANIZATION NAME AND ADDRESS Department of Mechanical Engineering University of Minnesota, Minneapolis, MN 55455		10. PROGRAM ELEMENT, PROJECT, TASK AREA & WORK UNIT NUMBERS Work Unit NR097-437
11. CONTROLLING OFFICE NAME AND ADDRESS Office of Naval Research 800 North Quincy Street Arlington, Virginia 22217		12. REPORT DATE January, 1982
		13. NUMBER OF PAGES 102
14. MONITORING AGENCY NAME & ADDRESS (if different from Controlling Office)		15. SECURITY CLASS. (of this report) Unclassified
		15a. DECLASSIFICATION/DOWNGRADING SCHEDULE
16. DISTRIBUTION STATEMENT (of this Report) Approved for public release; distribution unlimited		
17. DISTRIBUTION STATEMENT (of the abstract entered in Block 20, if different from Report)		
18. SUPPLEMENTARY NOTES		
19. KEY WORDS (Continue on reverse side if necessary and identify by block number) Heat exchangers, flow maldistribution, heat transfer coefficient, pressure drop, tube bank, plenum chamber, swirl		
20. ABSTRACT (Continue on reverse side if necessary and identify by block number) <p>The details of five separate but interrelated research problems are described in this report. The general theme which runs through the work is a search for the effects of flow maldistribution on heat transfer in various types of heat exchange devices. The research includes both experiment and analysis and deals with turbulent flows,</p> <p>The first of the experiments is concerned with the heat transfer</p>		

and pressure drop response of a tube bank to maldistribution of the flow at the inlet cross section. The maldistribution was created by a partial blockage of the inlet. In the second experiment, local turbulent heat transfer coefficients for airflow were measured in a tube situated downstream of a cylindrical plenum chamber in which the inflow was radial and the outflow was axial. This configuration requires that the air turn as it passes through the plenum, thereby inducing a highly complex flow at the tube inlet, as documented by flow visualization. The third experiment also deals with maldistribution, in particular, that created when there is a missing tube in a staggered or in-line tube bank. ✓

The computational work is concerned primarily with fluid flow aspects. In one of the investigations, predictions are made of the turbulent flow field and the associated pressure drop in a cylindrical plenum. The second computational study yields a prediction of flow maldistribution in a tube bundle placed in a flow with a sudden expansion.

Accession For	
NTIS GRA&I	<input checked="" type="checkbox"/>
DTIC TAB	<input type="checkbox"/>
Unannounced	<input type="checkbox"/>
Justification	
By	
Distribution/	
Availability Codes	
Dist	Avail and/or Special
A	



Unclassified

TABLE OF CONTENTS

	Page
Introduction to the Report	1
Chapter 1: Effect of Blockage-Induced Flow Maldistribution on the Heat Transfer and Pressure Drop in a Tube Bank . . .	3
Chapter 2: Heat Transfer and Fluid Flow Experiments with a Tube Fed by a Plenum Having Nonaligned Inlet and Exit	37
Chapter 3: Effect of a Missing Cylinder on Heat Transfer and Fluid Flow in an Array of Cylinders in Crossflow	71
Chapter 4: Prediction of the Turbulent Flow in a Cylindrical Plenum	85
Chapter 5: Prediction of Flow Maldistribution in a Tube Bundle Placed in a Flow with Sudden Expansion	95

INTRODUCTION TO THE REPORT

Heat exchange that occurs in power producing systems is significantly affected by the highly complex fluid flows that are encountered in such systems. For example, maldistributed flows occur almost as a matter of course in heat exchangers, a case in point being Navy shipboard heat recovery utilizing gas turbine exhaust. The complexity of the flow and the resulting maldistribution may result from changes of flow cross section, partial blockage due to valves and other control devices, branching or merging of flow passages, and changes in direction due to bends and elbows. Often, several of these features occur in a single system. In addition to maldistribution, the resulting flows may contain regions of flow separation, recirculation, and swirl.

The heat transfer characteristics of such flows are fundamentally different from those of conventional flows. Consequently, it is inappropriate to use available information for conventional flows as a basis for the heat transfer design of systems which experience complex flows. Thus, for example, large variations of the local heat transfer coefficient can be expected in complex flows, in contrast to the relatively uniform coefficients for conventional flows. Furthermore, such variations may give rise to local hot spots. In regions of flow separation and recirculation, the heat transfer coefficients may either be larger or smaller than those of an ordinary unidirectional flow, depending on the Reynolds number. In addition to marked effects on the heat transfer coefficient, the complexity of the flow also leads to significant increases in pressure drop.

The foregoing discussion serves to motivate and focus the research that is described in this report. The general theme which runs through the work is a search for the effects of flow maldistribution on heat transfer in various generic types of heat exchange devices. All told, five separate but interrelated research problems are described--three experimental and two computational. The first of the experiments deals with the heat transfer and pressure drop response

of a tube bank to maldistribution of the flow at the inlet cross section. The maldistribution was created by a partial blockage of the inlet cross section. In the second experiment, local turbulent heat transfer coefficients for airflow were measured in a tube situated downstream of a cylindrical plenum chamber in which the inflow was radial and the outflow was axial. This configuration requires that the air turn as it passes through the plenum, thereby inducing a highly complex flow at the tube inlet, as documented by flow visualization. The third experiment also deals with maldistribution, in particular, that created when there is a missing tube in a staggered or in-line tube bank.

The computational work is concerned primarily with fluid flow aspects. In one of the investigations, predictions are made of the turbulent flow field and the associated pressure drop in a cylindrical plenum. The second computational study yields a prediction of flow maldistribution in a tube bundle placed in a flow with a sudden expansion.

Chapter 1

EFFECT OF BLOCKAGE-INDUCED FLOW MALDISTRIBUTION
ON THE HEAT TRANSFER AND PRESSURE DROP IN A TUBE BANK

ABSTRACT

Detailed experiments, encompassing per-tube heat transfer measurements and row-by-row pressure measurements, were performed to investigate the response of a tube bank to maldistribution of the flow at the inlet cross section. The maldistribution was created by a partial blockage of the inlet section. Baseline experiments for uniformly distributed inlet flow were also carried out. The experiments spanned an order of magnitude range in the Reynolds number. On the whole, the inlet-section flow maldistribution tends to enhance the heat transfer at a given Reynolds number. Enhancements in the 30 - 40 percent range are encountered in the first several rows in the corridor downstream of the unblocked portion of the inlet section. Reductions (up to 50 percent) are confined to a narrow alley behind the blockage. Ten percent maldistribution-related effects persist to the seventh row, while effects at the five percent level occur at least as far downstream as the twelfth row. With regard to pressure, there is an incremental pressure drop of about $2\frac{1}{2}$ velocity heads due to the maldistribution.

NOMENCLATURE

A_{\min}	minimum free flow area
A_{naph}	per-tube mass transfer area
D	tube diameter
D	naphthalene-air diffusion coefficient
f	friction factor, equation (11)
K	per-tube mass transfer coefficient, $\dot{m}/(\rho_{\text{nw}} - \rho_{\text{nb}})$

ΔM	per-tube change of mass
\dot{m}	per-tube rate of mass transfer per unit area
N	row number
Nu	Nusselt number
Pr	Prandtl number
p	pressure
p_{∞}	pressure upstream of array
Δp	pressure drop, $(p_{\infty} - p(x))$
Re	Reynolds number, $\rho V D / \mu$
Sc	Schmidt number
Sh	per-tube Sherwood number, KD / \mathcal{D}
S_L	longitudinal pitch
S_T	transverse pitch
V	characteristic velocity, $\dot{w} / \rho A_{\min}$
\dot{w}	rate of fluid flow through array
x	axial coordinate
μ	viscosity
ν	kinematic viscosity
ρ	air density
ρ_{nb}	naphthalene vapor density in bulk flow
ρ_{nw}	naphthalene vapor density at tube surface
τ	duration of data run

INTRODUCTION

Flow maldistribution is a widely encountered operational problem in heat exchanger practice. In general, maldistributions may be classified in two categories, depending on whether the fluid flow which enters the heat exchanger is maldistributed or whether the maldistribution is induced within the heat exchanger itself. The focus of the present report is on maldistributed entering flows, illustrations of which will be described shortly. Internally induced maldistributions are caused by geometrical irregularities and imperfections, which give rise, for example, to leakage and bypass in shell and tube heat exchangers, and by differential heating, which is of particular relevance in laminar heat exchangers employing viscous liquids.

There are numerous causes of possible maldistributions in the flow that is delivered to the inlet cross section of a heat exchanger. If the inlet were situated downstream of a bend or an elbow, the nonuniform packing of the flow in the bend would be reflected in a nonuniform distribution across the inlet. Furthermore, secondary motions (i.e., corkscrew-like motions) are generated in bends and turns, and such motions further complicate the flow entering the heat exchanger. Overly rapid enlargements of the duct work which feeds a heat exchanger will give rise to zones of flow separation and recirculation which are carried into the exchanger inlet. Partially open valves and misaligned baffles are sources of nonuniform flow, and the eddies shed from these devices constitute a further degree of complexity. In applications where a heat exchanger is fed from the exhaust of a rotating device such as a gas turbine, there will be a strong swirl superposed on the inlet flow.

The foregoing slate of physical situations which favor maldistributed inlet flows is illustrative rather than exhaustive. Furthermore, the agents causing maldistribution are often compounded, for example, a swirling flow delivered to a heat exchanger via a bend and an overly rapid enlargement.

Waste heat recovery systems, which have become an essential factor in effective energy management, are especially vulnerable to pathological ducting arrangements for delivery of hot gases to the heat exchanger inlet. This is because such systems are often retrofited in an existing plant site and, as a consequence, both the ductwork and the heat exchanger have to be adaptive to the available space. Even in new installations, the size of waste heat systems and the cost of physical space often leads to nonideal ducting arrangements.

The importance of maldistributed inlet flows is widely recognized among heat exchanger practitioners (e.g., {1, 2}), but the complexity of the problem appears to have been a deterrent to research at a fundamental level. The work reported in the published literature is mainly focused on estimating the effects of the maldistribution by employing analytical models in which the heat transfer coefficients, needed as input, are based strictly on assumption (e.g., {3 - 6}). In some cases, heat transfer coefficients for uniformly distributed flows have been employed, while in others, a simple power-law relation between the transfer coefficient and the mass velocity is assumed to hold. It does not appear that detailed measurements have heretofore been made of the transfer coefficients in heat exchangers subject to a maldistributed inlet flow.

In the research to be reported here, experiments are performed in which, seemingly for the first time, heat transfer coefficients are measured internal to a heat exchanger with a maldistributed inlet flow. In planning the research program, it appeared most appropriate to model a generic type of maldistribution rather than to reproduce one of the myriad of specific maldistribution arrangements that occur in practice. The heat exchanger configuration to be studied here is, itself, generic--a tube bank through which air passes in crossflow. Attention will be focused on the heat transfer characteristics of the flow external to the tubes (in contrast to the internal flow).

The special feature of the research is that heat transfer coefficients were

measured at each of the individual tubes of the array. These detailed measurements were performed for both the maldistributed flow and for the case of a uniformly distributed flow, both at the same Reynolds number. The per-tube heat transfer coefficients in the presence of the maldistribution were ratioed with the corresponding coefficients for the uniform flow. The deviation of each ratio from unity provides an immediate index of the effect of the maldistributed inlet flow in either degrading or enhancing the per-tube heat transfer coefficient.

The aforementioned ratios are presented on a plan view of the tube bank, with each tube being inscribed with its individual ratio. In this presentation, zones of enhancement and degradation are readily identified. In addition, the propagation of the inlet section maldistribution through the heat exchanger can be observed, as can the homogenization of the flow as the maldistribution wanes.

In the experiments, the maldistribution was created by a partial blockage of the inlet cross section of the heat exchanger. Owing to the inability of the entering flow to turn sharply and fill the space downstream of the blockage, a low-velocity recirculation zone is set up. On the other hand, the flow passing through the unobstructed portion of the inlet section creates an alley of relatively high velocity fluid that penetrates the heat exchanger. To create a severe case of maldistribution, the experiments were performed with an inlet-section blockage of fifty percent. The Reynolds number was varied over an order of magnitude during the course of the experiments.

In order to obtain the detailed information described in the foregoing, it was found advantageous to perform mass transfer experiments rather than direct heat transfer experiments. The naphthalene sublimation technique was used in the mass transfer experiments, and the mass transfer coefficients were converted to heat transfer coefficients by employing the analogy between the two processes. As the first order of business in the experimental program, the validity of the analogy was examined by comparisons of the present results for uniform inflow with well-

established results in the heat transfer literature. The remarkable level of agreement that emerged from these comparisons provides unassailable support for the use of the analogy in heat exchanger work.

In addition to the heat/mass transfer studies, the pressure drop was measured as a function of position along the length of the heat exchanger, both for the maldistributed and uniform flow cases. The comparison of the results enables identification of the incremental pressure drop due to the flow maldistribution. These multi-station internal pressure measurements represent a departure from conventional heat exchanger practice where pressure measurements are made only before and after the exchanger.

THE EXPERIMENTS

Experimental apparatus. The description of the experimental apparatus is facilitated by reference to Figs. 1 - 3. The first of these is a photograph of the test section and related downstream ductwork (hereafter designated as the afterduct). Figures 2 and 3 are schematic diagrams showing various details of the test section.

In Fig. 1, the test section is the portion of the apparatus that is forward of the flange. The photograph was taken with the inlet cross section unblocked, and the first row of tubes can be seen through the open inlet. Another feature of the test section that is evident in Fig. 1 is that the top wall is removable. In connection with the removable top, there are three quick-release clamps affixed to the upper edge of the respective side walls. When the clamps are closed, they bear down on the top wall, causing it to seal against O-rings. With the opening of the clamps, the top wall can be removed in a matter of seconds with the aid of the specially machined handles that are attached to the wall. A row of static pressure taps, deployed along the spanwise centerline of the top wall, can also be seen in Fig. 1.

Figure 2 is a schematic diagram of the front face of the test section, with the blockage in place (but shown as semi-transparent in order to reveal the parts

that are situated behind the blockage). As seen in the figure, the test section is a square duct whose lower and side walls were fabricated from thick aluminum plates (2.54 cm, 1 in.) to enable laps to be cut for interleaving the walls and ensuring precise positioning. Laps at the outer edges of the bottom wall provided seating for the side walls and, in turn, laps at the upper edges of the side walls seated the top wall. These laps also served as flats into which the O-ring grooves were milled. All surfaces of the duct walls which interface with the airflow were painstakingly polished with 600-grit wet or dry sandpaper (used wet) as the final step of the fabrication process.

The spanwise arrangement of the tubes in the first row can be seen in Fig. 2. This arrangement, which is repeated in the third, fifth, and all other odd rows, includes five regular tubes (away from the side walls) and a half tube adjacent to each of the side walls. The wall-adjacent half tubes were employed to more closely model an infinitely wide array, and the success of this approach will be documented later.

A plan view of the test section with the top wall removed and without the blockage in place is presented in Fig. 3; also, for clarity, the quick-opening clamps are not shown. This figure illustrates the layout of the tube bank. The tubes are seen to be positioned in a staggered array, with six tubes in each row. Precise, positive positioning of the tubes was ensured by seating them in holes that had been drilled into the lower wall of the duct. The aforementioned wall-adjacent half tubes situated in the odd numbered rows are seen, in actuality, to be regular tubes that are recessed into the side walls so that only half of each tube is exposed to the airflow.

Further study of the figure shows that the tubes are positioned on equilateral triangular centers. The transverse center-to-center distance S_T between the tubes was chosen to be twice the tube diameter D (i.e., $S_T/D = 2$). The corresponding longitudinal pitch-to-diameter ratio $S_L/D = (\sqrt{3}/2)S_TD = 0.866(S_T/D)$. The array

employed in the experiments contained 15 rows of tubes, as pictured in the figure. The portion of the test section aft of the array served as a downstream plenum chamber.

The experiments will be characterized in dimensionless terms so that the test section dimensions are relevant only for orientation purposes. The cross section is a 7.62 x 7.62 cm (3 x 3 in.) square. Each tube is 0.635 cm (0.250 in.) in diameter and 7.62 cm (3 in.) in length, and the transverse pitch S_T is 1.27 cm (0.500 in.). The 12:1 aspect ratio of the tube is sufficient to eliminate concern about mass transfer end effects, especially since there is zero mass transfer at the duct walls (the duct walls are metallic and, therefore, do not participate in the mass transfer process). It should be noted that in a corresponding heat transfer experiment, the end effects would, in all likelihood, be greater due to both conductive and convective interactions between the tubes and the duct walls.

As indicated in the Introduction and illustrated in Fig. 2, the selected blockage element constricted half of the inlet cross section. In considering a plate to serve as the blockage element, it was recognized that flow separation would occur at its exposed edge (i.e., the left-hand edge of the element pictured in Fig. 2). To achieve a sharply defined separation, a thin brass plate was used (0.020 cm, 0.008 in.). It was verified that the plate, when in place, did not deform under the action of the forces exerted by the airflow.

For the determination of the pressure distribution along the test section, twelve regularly spaced pressure taps were installed along the spanwise centerline of the top wall, as seen in Fig. 1. The first tap is positioned midway between the second and third rows of tubes, 2.750 cm (1.083 in.) from the leading edge of the duct. All subsequent taps are separated by an axial distance of $2S_L$ ($= 2.200$ cm, 0.866 in.).

In addition to the regular top wall of the test section, a special top wall was fabricated and used during a preparatory stage of each data run. During that

stage, it is necessary to pass air through the test section for a preselected time so that thermal equilibrium is achieved between the naphthalene mass transfer element and the flow. During this equilibration period, the mass transfer element is jacketed by a teflon cover which protrudes above the top of the test section. The special top wall contains an elevated section which accommodates the protruding portion of the jacket. Furthermore, the elevated section can be positioned at any axial station to accommodate a mass transfer element situated in any row of the array.

In the fully assembled experimental apparatus, air was drawn from the temperature-controlled laboratory into the inlet of the test section. The air traversed the test section and exited into the afterduct (Fig. 1), which served as a transition piece between the square test-section geometry and the circular downstream piping. The afterduct was designed to be sufficiently long so that the contraction experienced by the flow at the downstream end of the duct (i.e., as the flow entered the downstream circular piping) was not felt in the test section. From the afterduct, the flow passed into a metering section (two calibrated rotameters), through a control valve, and then was ducted to the blowers. The blowers were situated in a service corridor outside the laboratory, and their exhaust was vented to the outdoors. The capacity of the air-handling system was 130 scfm. Experiments were performed over the range from 13 to 130 scfm.

The operation of the system in the suction mode and the placement of the blowers outside the laboratory, together with the room temperature control, enabled the attainment of steady, readily measurable operating temperatures in the test section--a necessary prerequisite for the naphthalene sublimation technique. Also, the outside exhaust, coupled with strict handling procedures, ensured that the laboratory was free of naphthalene vapor.

Tubes and naphthalene test element. Each tube is, in actuality, a solid cylinder machined with a shank of smaller diameter at one end to facilitate its

seating in the lower wall of the test section. To ensure uniformity of diameter for all the cylinders, they were fabricated from 0.635 cm (0.250 in.) drill rod. The length of each cylinder was machined so that the clearance between the tip of the cylinder and the top wall of the test section was 0.0025 - 0.005 cm (0.001 - 0.002 in.).

In each data run, only one of the cylinders in the array participated in the mass transfer process. The participating cylinder was a composite consisting of a naphthalene coating enveloping a metal substrate. The first step in the fabrication of a coated cylinder was to reduce the diameter of the body of one of the aforementioned standard cylinders by about 3/4 mm. Following the under-cutting operation, the resulting surface was machined so as to form a 1/4-mm deep screw thread. The purpose of the screw thread was to provide cavities to aid in the adhesion of the naphthalene. The thus-machined cylinder was dipped into a container of molten naphthalene, the dipping process being performed in many stages so that the surface temperature was kept low enough to avoid remelting of the naphthalene that had solidified on it. Once a sufficiently thick coating had been built up, the coated cylinder was machined in a lathe to remove the excess solidified naphthalene. The machining was continued until the diameter of the naphthalene-coated cylinder was equal to the diameter of the uncoated cylinders of the array. The tip was machined to completely remove the solidified naphthalene.

For efficiency in executing the experiments, it was standard practice to coat and machine at least eight to ten cylinders at a time. Upon completion of the coating process, the cylinders were wrapped in impermeable plastic and placed in the laboratory where the experiments were to be conducted. A freshly prepared coated cylinder was employed for each data run (i.e., coated cylinders were never reused). Subsequent to each data run, the remaining naphthalene coating was removed by melting and evaporation in preparation for the next round of coating and machining operations.

Experimental procedure and instrumentation. The key measurements made during a mass transfer data run included the mass of the naphthalene-coated cylinder, the temperature of the air entering the test section, the airflow rate, and the barometric pressure. The mass measurements were made with a Sartorius analytical balance with a resolution of 0.0001 g and a capacity of 200 g. Air temperature was sensed by an ASTM-certified thermometer with a smallest scale division of 0.1°F. As noted earlier, calibrated rotameters equipped with static pressure taps were employed for the airflow measurements.

In supplementary runs (without mass transfer) made to determine the pressure drop characteristics of the array, the pressure signals from the test-section static taps were conveyed to a specially fabricated selector switch. The output of the switch was fed to the terminals of a Baratron solid-state, capacitance-type pressure meter capable of resolving 10^{-4} mm Hg at levels of 1, 10, and 100 Hg, depending on the sensing head employed.

Certain aspects of the experimental procedure have already been mentioned, and additional relevant details will now be described. To prepare for a data run, the room lighting and the blowers in the air-handling system were turned on at least thirty minutes before the intended start of the run. A steady temperature was thereby established and subsequently maintained to within 0.05 - 0.1°C during the data run by the temperature control system of the room.

The next preparatory step involved the attainment of thermal equilibrium between the naphthalene-coated cylinder and the airflow passing through the array. The attainment of temperature equality is a necessary prerequisite for the evaluation of the naphthalene surface temperature from the measured air temperature. To attain the desired equilibrium, the naphthalene-coated cylinder, jacketed in a close-fitting sealed teflon sleeve to minimize extraneous sublimation, was inserted at a pre-selected position in the array. The cylinder was allowed to remain in the array for about 30 minutes, during which time it was exposed to the

airflow rate that had been set for the data run. After the equilibration period, the cylinder was removed from the array, weighed on the analytical balance (with teflon jacket removed), and then returned (with jacket in place) to the array for an additional 5 - 10 minute equilibration period.

The mass transfer period was initiated by the removal of the teflon jacket, thereby exposing the naphthalene-coated cylinder to the airflow. During the run, readings of temperature, flow rate, rotameter pressure, and barometric pressure were taken at regular intervals. The duration of the run was chosen so that the average change of thickness of the naphthalene coating due to sublimation would be about 0.0025 cm (0.001 in.), equivalent to about a 0.05 g mass loss. To terminate the run, the naphthalene-coated cylinder was jacketed, removed from the array, and weighed (with jacket removed).

At this point, a supplementary data run was carried out to determine a correction for any extraneous mass transfer that may have occurred in the period between the first and second weighings. All of the steps that had been performed between the first and second weighings were repeated, except for the exposure to the airflow, and following this, a third weighing was made. The thus-determined correction was on the order of one percent of the net mass transfer.

DATA REDUCTION

The procedures employed to evaluate the per-tube Sherwood number (i.e., the mass transfer counterpart of the Nusselt number), the Reynolds number, and the pressure drop coefficient will now be described. For the Sherwood number determination, the first step is to obtain the per-tube mass transfer coefficient K from its definition

$$K = \dot{m} / (\rho_{nw} - \rho_{nb}) \quad (1)$$

in which \dot{m} is the per-tube mass transfer per unit time and area, and ρ_{nw} and ρ_{nb} denote the densities of naphthalene vapor at the tube surface and in the bulk

airflow. The quantity \dot{m} was determined from the measured mass loss ΔM due to sublimation from the surface of the naphthalene-coated cylinder and from the duration τ of the data run and the area A_{naph} of the naphthalene surface, so that

$$\dot{m} = \Delta M / \tau A_{\text{naph}} \quad (2)$$

In evaluating A_{naph} , account was taken of the slight change in the cylinder diameter during the data run.

The naphthalene vapor density ρ_{nw} was evaluated by a two-step process. In the first step, the naphthalene vapor pressure at the cylinder surface was calculated from the Sogin vapor pressure--temperature relation {7}. Then, the vapor density was determined from the perfect gas law. In these calculations, it was assumed that the surface temperature of the naphthalene coating was equal to the temperature of the air passing through the tube array. The general validity of this assumption was ensured by the equilibration period which preceded each data run.

There are, however, two possible causes of a small temperature difference between the surface and the air. The first is related to the fact that the latent heat of sublimation must be supplied to sustain the mass transfer process and, if the heat were supplied by the airstream, a temperature difference must exist. The maximum possible difference due to this process was calculated to be 0.09°C . The second possible cause of temperature difference arises from the fact that the airstream thermometer measures the stagnation temperature while the naphthalene surface is at the recovery temperature. For a recovery factor of 0.8, the maximum difference between the stagnation and recovery temperatures was found by calculation to be 0.044°C . The maximum temperature difference due to the aforementioned causes is about 0.13°C , which corresponds to a maximum uncertainty of 1.3 percent in the results. This uncertainty was judged to be tolerable.

Once the mass transfer coefficient is evaluated from equations (1) and (2),

it may be recast in dimensionless form in terms of the Sherwood number Sh

$$Sh = KD/\mathcal{D} \quad (3)$$

where D is the tube diameter and \mathcal{D} is the naphthalene-air diffusion coefficient.

The latter may be eliminated by taking note of the definition of the Schmidt number Sc , which is the mass transfer counterpart of the Prandtl number. Since $Sc = \nu/\mathcal{D}$, equation (3) becomes

$$Sh = (KD/\nu)Sc \quad (4)$$

in which ν is the kinematic viscosity of air and $Sc \approx 2.5$ for naphthalene diffusion in air.

The Reynolds number definition used to characterize the experiments is that which is standard for tube banks. If \dot{w} is the rate of airflow through the array and A_{\min} is the minimum free-flow area, then $\rho V = \dot{w}/A_{\min}$ and

$$Re = \rho V D / \mu \approx \dot{w} D / \mu A_{\min} \quad (5)$$

Attention will now be turned to the analogy between heat and mass transfer. For heat transfer in a tube bank, it is customary to correlate data in the form

$$Nu = C Re^m Pr^n \quad (6)$$

For mass transfer in a geometrically similar tube bank, the mass transfer counterpart of equation (6) is

$$Sh = C Re^m Sc^n \quad (7)$$

where the quantities C , m , and n are the same in equations (6) and (7). Thus,

$$Nu = (Pr/Sc)^n Sh \quad (8)$$

which enables the Sherwood number results to be transformed to Nusselt numbers.

The theoretical basis of the analogy is set forth in {8}. An experimental verification will be presented shortly. In view of the analogy, heat transfer and mass transfer terminology will be used interchangeably.

For the presentation of the pressure drop results, the quantity ΔP is defined as

$$\Delta p = p_{\infty} - p(x) \quad (9)$$

where p_∞ is the pressure upstream of the test section and $p(x)$ is the pressure at an axial station x . A dimensionless presentation may be attained by the ratio

$$\Delta p / \frac{1}{2} \rho V^2 \quad (10)$$

with $\rho V^2 = \dot{m}^2 / \rho A_{\min}^2$, and ρ is the average density in the test section. For comparisons with the literature, a friction factor will be defined later.

RESULTS AND DISCUSSION

Heat (mass) transfer results for uniform inlet flow. The results to be reported first are those corresponding to a uniformly distributed inlet flow. These results will be compared with appropriate heat transfer results from the literature with a view both to confirming the validity of the heat-mass transfer analogy and to demonstrating the propriety of the experimental apparatus and technique. Subsequently, the uniform-inlet-velocity results will be used as a baseline for comparison with the results for the maldistributed inlet flow.

Figure 4 shows a comparison of the present uniform-inlet-flow results with those of the literature, with the Sherwood number plotted as a function of the Reynolds number. Comparisons are made both for the first-row Sherwood numbers and for the fully developed Sherwood numbers (the fully developed regime will be elaborated upon shortly).

To represent the heat transfer literature, the widely quoted tube-bank correlation of Grimison {9} will be used. Grimison's correlation is based on air data ($Pr = 0.7$), and it has become customary to scale his results to other Prandtl (or Schmidt) numbers by a $Pr^{1/3}$ (or $Sc^{1/3}$) factor (e.g., {10}). Thus, using equation (8), Grimison's Nusselt numbers were converted to Sherwood numbers by the relation $Sh = (2.5/0.7)^{1/3} Nu$. The Grimison correlation is applicable to the fully developed regime, and for the thermal entrance regime it is standard to use the Kays-Lo correlation factors {11}, as was done here. In addition, the stated range of the Grimison correlation is $Re > 2000$. Consequently, dashed lines have

been used in the plotting of his correlation for $Re < 2000$.

Examination of Fig. 4 indicates that the present mass transfer data are in excellent agreement with the heat transfer literature. In the range above $Re = 2000$, where the Grimson correlation is valid, the maximum deviation is three percent, which is much less than the scatter of the heat transfer data on which the correlation is based. Even below $Re = 2000$, very good agreement prevails, especially in the fully developed regime. The remarkable agreement evidenced in Fig. 4 confirms both the heat-mass transfer analogy and the present experimental technique.

Attention is now turned to the row-by-row variation of the per-tube Sherwood number. This information is conveyed in Fig. 5 for the three Reynolds numbers for which nonuniform-inlet-flow results will be presented later. These Reynolds numbers are equally spaced logarithmically over an order of magnitude. The figure shows the expected increase of the Sherwood number in the initial rows, as the turbulence spawned by the tubes themselves enhances the mass (heat) transfer in downstream rows. However, a periodic fully developed regime soon sets in wherein the fluid flow about each tube is the same from row to row. As a consequence, the Sherwood number becomes a constant, independent of the row number.

For the higher Reynolds numbers, row-independent Sherwood numbers are in evidence in the third and subsequent rows, while for the lowest Reynolds number thermal development was achieved at the fourth row. These development lengths reflect the rapidity with which the velocity field attains its periodic fully developed regime. The horizontal lines threaded through the fully developed data represent average values, respectively equal to $Sh = 28.8$, 58.3 , and 118 for $Re = 850$, 2750 , and 8400 .

The final matter to be considered with respect to the uniform-inlet-flow experiments is the spanwise uniformity of the Sherwood numbers in any given row, and Table 1 has been prepared in this connection. The table shows the per-tube

Sherwood numbers at each of the six tubes that are deployed across the span of the eighth row, respectively for $Re = 850$, 2750 , and 8400 . Relative to the respective

Table 1
Spanwise Sherwood Number Distribution in the Eighth Row

Re	Spanwise Position					
	1	2	3	4	5	6
850	28.3	28.1	28.6	28.4	28.6	27.8
2750	56.9	57.6	57.5	58.5	58.4	56.0
8400	117	119	118	118	119	118

averages, the data scatter by 1 - 2 percent, which is the estimated accuracy of the results. Furthermore, there is not a consistent pattern in the observed spanwise variations, which suggests that wall effects, if present, are very small. Within the scatter of the data, it is believed that the data can, for practical purposes, be regarded as spanwise uniform.

Heat (mass) transfer results for maldistributed inlet flow. As discussed earlier, the flow maldistribution studied here was created by a blockage which closed off half the inlet cross section, as illustrated in Fig. 2. The presence of the maldistribution destroyed the spanwise uniformity that had existed for the unblocked case, necessitating separate mass transfer measurements for each tube in a given row. Such measurements were made for each tube in the first eight rows and for the tubes of the twelfth row, all for $Re = 850$, 2750 , and 8400 .

The results will be presented in a format which provides an immediate visual image of the effects of the maldistribution. To this end, the Nusselt (Sherwood) number at a given tube in the presence of the flow maldistribution is ratioed with the uniform-inlet-flow Nusselt (Sherwood) number at the same tube. These ratios have been recorded adjacent to each tube in a top-view layout of the array. The

respective layouts for $Re = 850$, 2750 , and 8400 are presented in Figs. 6 - 8. The blocked portion of the inlet cross section is also indicated in these diagrams.

In assessing the results of Figs. 6 - 8, it should be noted that a Nusselt number ratio in excess of one indicates a local enhancement--that is, higher per-tube heat transfer for the maldistributed flow than for the uniform inlet flow. Conversely, a ratio that is less than one indicates a maldistribution-related reduction in heat transfer at the tube in question.

From an overall examination of the figures, a number of common characteristics can be identified. First of all, it appears that ratios in excess of one are more in evidence than those below one so that, on the whole, the maldistribution tends to enhance the heat transfer at a given Reynolds number (the pressure drop ramifications will be considered shortly). The most significant enhancements occur at tubes situated in the first several rows in the corridor downstream of the open portion of the inlet. However, enhancement also occurs at tubes that are adjacent to this corridor and which, geometrically speaking, are behind the blockage. Heat transfer degradation (i.e., ratios significantly lower than unity) is confined to a narrow alley that is behind the blockage and adjacent to the side wall of the duct. This alley terminates at the sixth row.

The greatest enhancement takes place at the tube situated in the middle of the first row. This tube, which is half shielded by the blockage, is washed by eddies which are generated by the sharp edge of the blockage plate. It is these eddies that are responsible for the high heat transfer coefficients. Aside from the 60 - 80 percent enhancement at the first-row middle tube, the highest enhancements, those in the inlet corridor, are in the 30 - 40 percent range. The greatest reduction, about 50 percent, consistently occurs at the wall-adjacent tube in the fourth row (not in the behind-the-blockage corner region, as might have been expected).

The relatively high heat transfer coefficients that are in evidence in the

inlet corridor are caused by the high velocities which result from the channeling of the flow by the blockage. Owing to the inability of the flow to turn sharply as it passes the blockage plate, there is a separated region behind the blockage which is responsible for the zone of relatively low coefficients.

With increasing downstream distance, the heat transfer coefficients generally tend toward their values for the uniform-inlet-flow situation, as witnessed by the proliferation of ratios in the neighborhood of unity. However, in the downstream rows (i.e., rows seven and eight), a modest spanwise nonuniformity emerges whose cross-sectional variation is opposite to that of the spanwise nonuniformity which prevails in the upstream rows. Specifically, lower coefficients occur in the unblocked corridor and higher coefficients occur behind the blockage. (This finding, initially unexpected, provided the impetus for the spanwise exploration reported in Table 1 for the case of the uniform inlet flow.)

The aforementioned reversal in the trend of the spanwise variation reflects the tendency of the fluid to move transversely from the inlet corridor into the downstream portion of the region behind the blockage. This transverse flow creates a modest downstream maldistribution which has a high-to-low velocity variation that is opposite to that at the inlet. The data for the twelfth row indicate that this secondary maldistribution is beginning to wane for the lower Reynolds numbers, as evidenced by the approach toward more uniform values of the heat transfer coefficient. At the highest Reynolds number, the secondary maldistribution has not yet begun to abate.

The foregoing discussion naturally leads to a consideration of the number of rows of the heat exchanger that are affected by the presence of flow maldistribution at the inlet. If the threshold of significant maldistribution-related effects is defined as a ten percent change in the heat transfer coefficient, then the influence of the maldistribution is seen to extend through the first seven rows of the heat exchanger. Lesser effects, at the five percent level, persist

at least as far as the twelfth row.

Although the results for the various Reynolds numbers display common trends, there are differences in detail. One of these is the slower development and subsequent slower disappearance of the aforementioned secondary maldistribution at higher Reynolds numbers. In addition, at lower Reynolds numbers, there is an overall trend toward lesser reductions in the heat transfer coefficient in the wall-adjacent region behind the blockage.

If per-row average values are calculated from the ratios displayed in Figs. 6 - 8, it is found that for all rows (except for a few 0.98 - 0.99 values for downstream rows), the row-average coefficient for the maldistributed flow exceeds that for the uniform flow. This finding offers quantitative testimony of the enhancing effect of the maldistribution on heat transfer (at a fixed Reynolds number). The first-row average is the highest among the various row averages for each Reynolds number, respectively equal to 1.30, 1.25, and 1.16 for $Re = 850$, 2750, and 8400. The percentagewise-greater enhancement for the lower Reynolds number is not unexpected.

Pressure drop and friction factor. A knowledge of the pressure drop is a necessary input for heat exchanger design and is of particular interest when the flow is maldistributed. The present approach to the determination of the pressure drop is much more detailed than that commonly employed for heat exchangers. In the conventional approach, the overall pressure drop is measured by taps situated fore and aft of the exchanger, and entrance and exit losses are calculated and subtracted away in order to obtain the pressure loss in the exchanger proper. In the present experiments, the pressure distribution within the heat exchanger is measured, and no corrections need be made.

The pressure distribution along the tube bank, plotted as $\Delta p / \frac{1}{2} \rho V^2$, is presented in Fig. 9, where $\Delta p = (p_\infty - p(x))$ and the velocity head $\frac{1}{2} \rho V^2$ is evaluated as indicated immediately following equation (10); p_∞ is the pressure upstream of the test section. The data for the unblocked-inlet case are shown in the lower

part of the figure, while that for the maldistributed inlet flow are plotted in the upper part of the figure. For each flow configuration, data are presented for $Re = 850, 2750, \text{ and } 8400$.

Attention may first be focused on the results for the unblocked inlet. As seen in the figure, the pressure distribution in the array is linear for all of the Reynolds numbers investigated (the flat portion of the distribution which follows the linear portion corresponds to the open duct downstream of the array). The linearity of the pressure distribution shows that fully developed conditions are established very near the inlet of the array. The fact that $\Delta p / \frac{1}{2} \rho V^2$ depends on the Reynolds number indicates that inertial losses, for which $\Delta p \sim \frac{1}{2} \rho V^2$ are not the sole contributor to the pressure drop, so that skin friction must also play a role.

To compare the present results with the literature, friction factors were evaluated from

$$f = (-dp/dN) / \frac{1}{2} \rho V^2 \quad (11)$$

where dp/dN , the pressure drop per row, is the slope of the least-squares straight line passed through the data. These friction factors are compared with those of Zukauskas {12} in Table 2 (only two significant figures could be read from

Table 2
Comparison of Friction Factors

Re	Present	{12}
850	0.362	0.36
2750	0.433	0.42
8400	0.456	0.48

the graphical presentation of {12}). The agreement evidenced by Table 2 is remarkable, especially in view of the differences in the experimental techniques

employed.

Turning next to the blockage case, it is seen that the presence of the maldistribution is felt up to about the sixth row. A pressure recovery is experienced by the flow after passing the blockage plate, as reflected by the negative slopes of the initial data points. Beyond the sixth row, a linear pressure variation is established. To examine this linear region, the slopes for the unblocked case have been transposed to the blocked case, and a good fit is found to prevail.

In the fully developed regime, a maldistribution-related incremental pressure drop of about $2\frac{1}{2}$ velocity heads persists.

CONCLUDING REMARKS

The work reported here is, seemingly, the first systematic experimental study of the effect of inlet-section flow maldistribution on the heat transfer and pressure drop characteristics of a heat exchanger. A special feature of the research is that heat transfer coefficients were measured at each of the individual tubes of the crossflow array. The maldistribution was created by a partial blockage of the inlet cross section of the heat exchanger. In baseline experiments for uniformly distributed entering flow, the measured transfer coefficients were found to be in excellent agreement with those in the heat transfer literature, thereby confirming both the heat-mass transfer analogy and the present experimental technique.

On the whole, the inlet-section flow maldistribution tends to enhance the heat transfer at a given Reynolds number. The most significant enhancements ($\sim 30 - 40$ percent) occur at tubes situated in the first several rows in the corridor downstream of the open portion of the inlet. Reductions of the heat transfer coefficient (up to 50 percent) are confined to a narrow alley that is behind the blockage and adjacent to the side wall of the heat exchanger. This alley terminates at the sixth row.

In the downstream rows of the heat exchanger, a secondary maldistribution develops whose spanwise variation is opposite to that which prevails in the upstream rows. This secondary maldistribution reflects the tendency of the fluid to move transversely from the inlet corridor into the downstream portion of the region behind the blockage.

The effect of the inlet-section flow maldistribution on the per-tube heat transfer coefficient subsides to ten percent or less after the seventh row. Lesser effects, at the five percent level, persist at least as far as the twelfth row.

The results for the various Reynolds numbers display common trends, with some differences in detail.

The measured pressure distributions along the heat exchanger yielded friction factors for the unblocked case which agreed very well with literature information. For the blockage case, the inlet-section flow maldistribution is felt up to the sixth row, whereafter a linear (fully developed) pressure variation is established. In the linear region, a maldistribution-related incremental pressure drop of about $2\frac{1}{2}$ velocity heads persists.

REFERENCES

1. London, A. L., "Compact Heat Exchangers--Design Methods," in Low-Reynolds-Number-Flow Heat Exchangers, Hemisphere Publishing Corporation, Washington, D.C., 1982.
2. Mueller, A. C., "Shell and Tube Exchanger Design," in Low-Reynolds-Number-Flow Heat Exchangers, Hemisphere Publishing Corporation, Washington, D.C., 1982.

3. Chiou, J. P., "Thermal Performance Deterioration in Crossflow Heat Exchanger Due to the Flow Nonuniformity," ASME Journal of Heat Transfer, Vol. 100, 1978, pp. 580-587.

4. Mueller, A. C., "An Inquiry of Selected Topics on Heat Exchanger Design," Donald Q. Kern Award Lecture, 16th National Heat Transfer Conference, August, 1976.

5. Dobryakov, B. A., "The Calculation of Heat Exchanger Equipment with Crossflow of the Heat Transfer Agents," International Chemical Engineering, Vol. 13, 1973, pp. 81-84.

6. Kutchev, J. A. and Julien, H.L., "The Measured Influence of Flow Distribution on Regenerator Performance," SAE Transactions, Vol. 83, Paper No. 740164, 1974.

7. Sogin, H. H., "Sublimation from Disks to Air Streams Flowing Normal to their Surfaces," Trans. ASME, Vol. 80, 1958, pp. 61-69.

8. Eckert, E. R. G., "Analogies to Heat Transfer Processes," in Measurements in Heat Transfer, E.R.G. Eckert and R. J. Goldstein, editors, Hemisphere Publishing Corporation, Washington, D.C., 1976.

9. Grimson, E. D., "Correlation and Utilization of New Data on Flow Resistance and Heat Transfer for Cross Flow of Gases over Tube Banks," Trans. ASME, Vol. 59, 1937, pp. 583-594.

10. Incropera, F. P. and DeWitt, D. P., Fundamentals of Heat Transfer, Wiley, New York, 1981, p. 355.

11. Kays, W. M. and Lo, R. K., "Basic Heat Transfer and Flow Friction Data for Gas Flow Normal to Banks of Staggered Tubes," Stanford University Technical Report No. 15, 1952.

12. Zukauskas, A. A., "Heat Transfer from Tubes in Crossflow," in Advances in Heat Transfer, Vol. 8, Academic Press, New York, 1972, pp. 154-155.

FIGURE CAPTIONS

- Fig. 1 Photograph of the test section and the afterduct
- Fig. 2 Schematic diagram of the front face of the test section
- Fig. 3 Plan view of the test section with the top wall removed
- Fig. 4 Comparison of Sherwood numbers for uniform inlet flow with those of the literature
- Fig. 5 Row-by-row variation of the Sherwood number for uniform inlet flow
- Fig. 6 Per-tube ratio of the maldistribution-affected Sherwood number to that for uniform inlet flow, $Re = 850$
- Fig. 7 Per-tube ratio of the maldistribution-affected Sherwood number to that for uniform inlet flow, $Re = 2750$
- Fig. 8 Per-tube ratio of the maldistribution-affected Sherwood number to that for uniform inlet flow, $Re = 8400$
- Fig. 9 Distributions of pressure along the tube bank

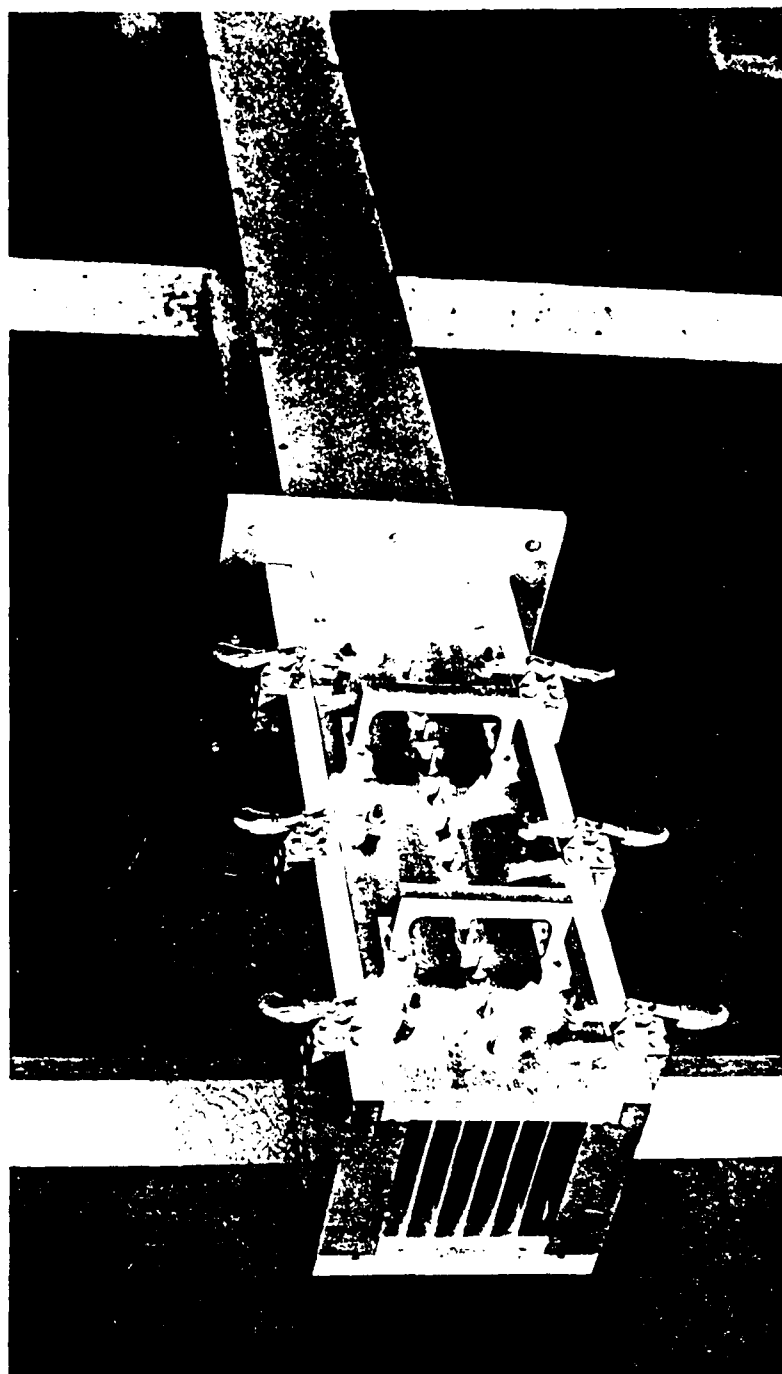


Fig. 1

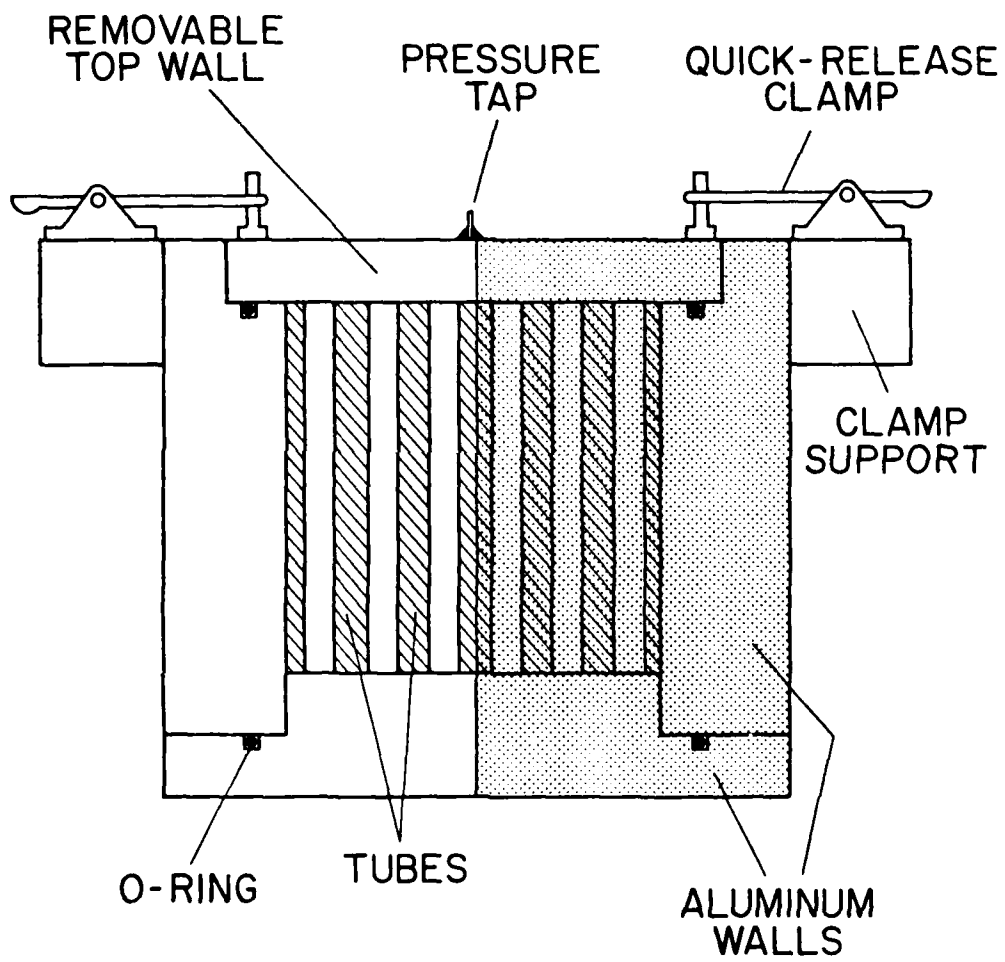


Fig. 2

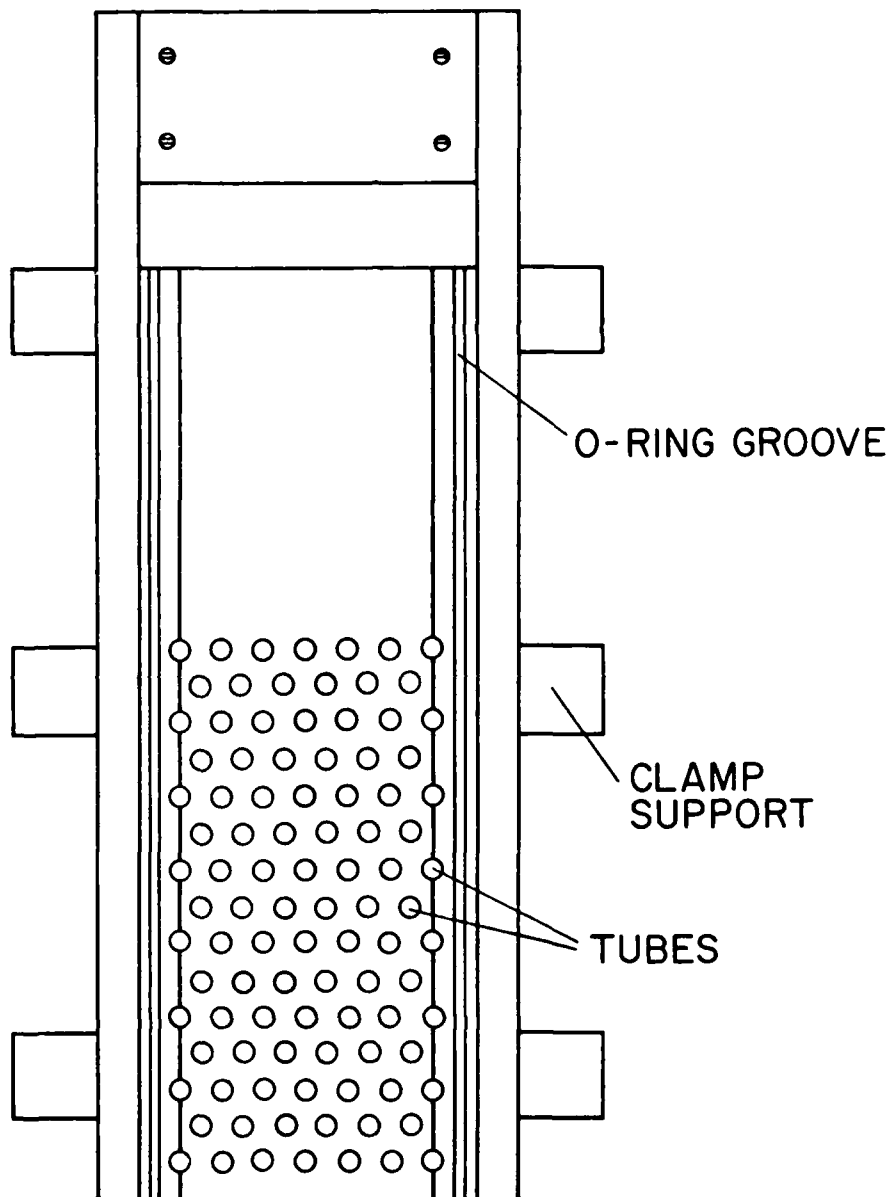


Fig. 3

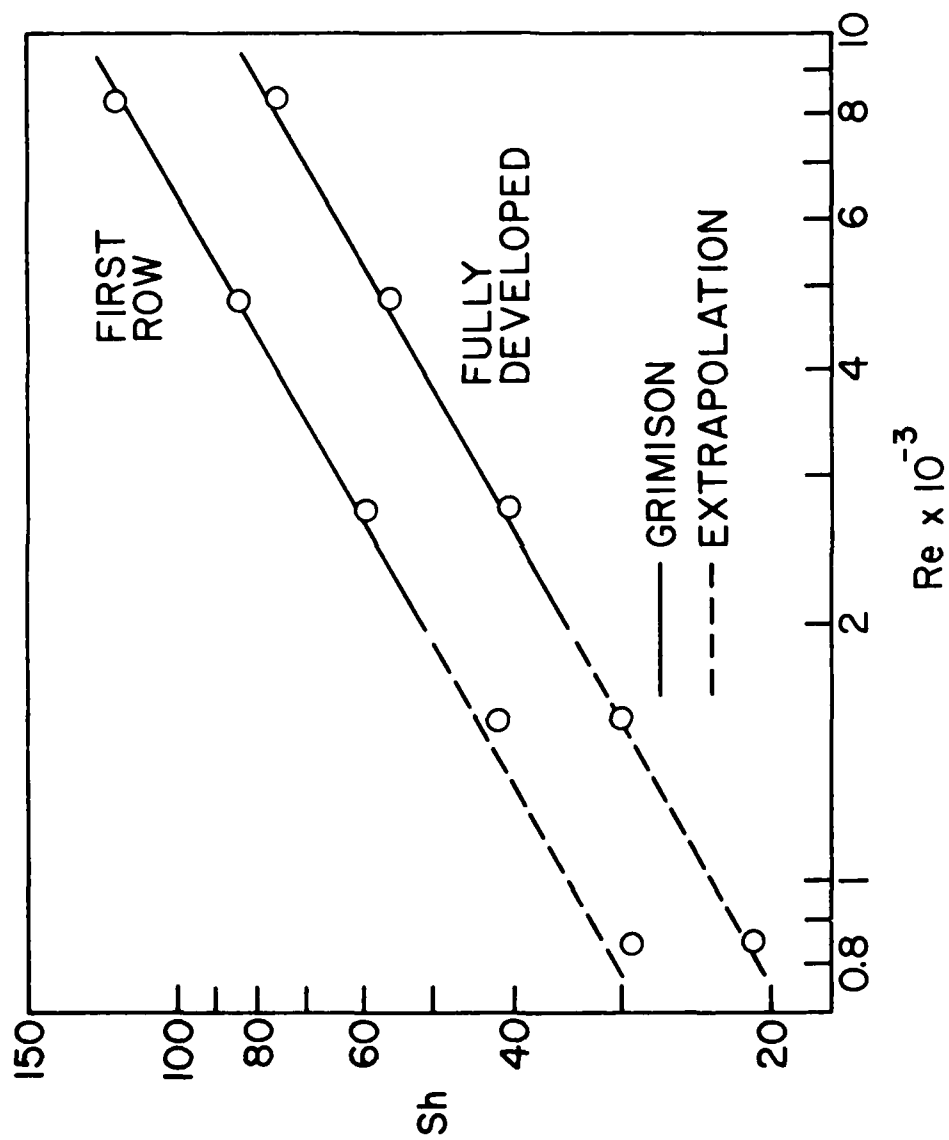


Fig. 4

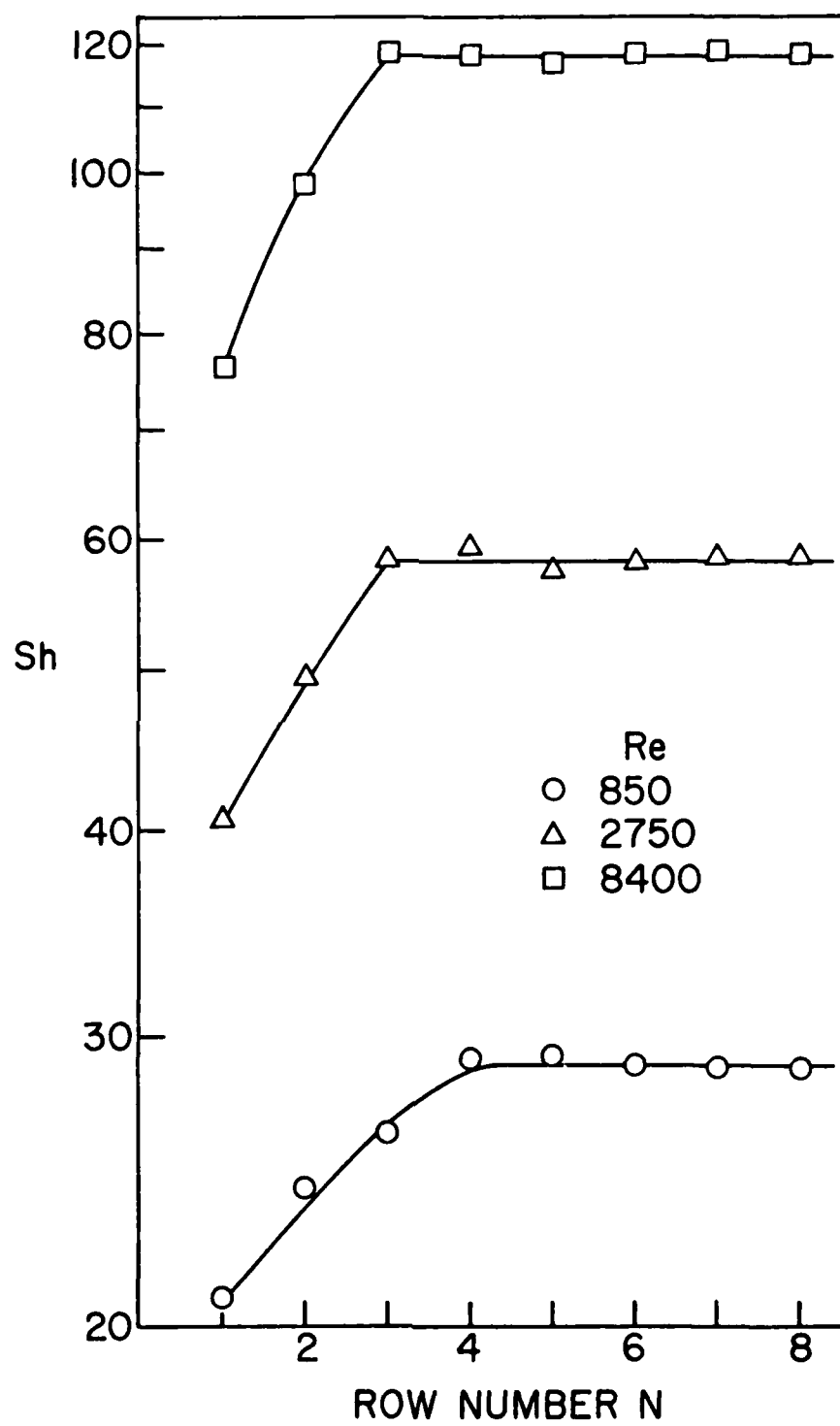


Fig. 5

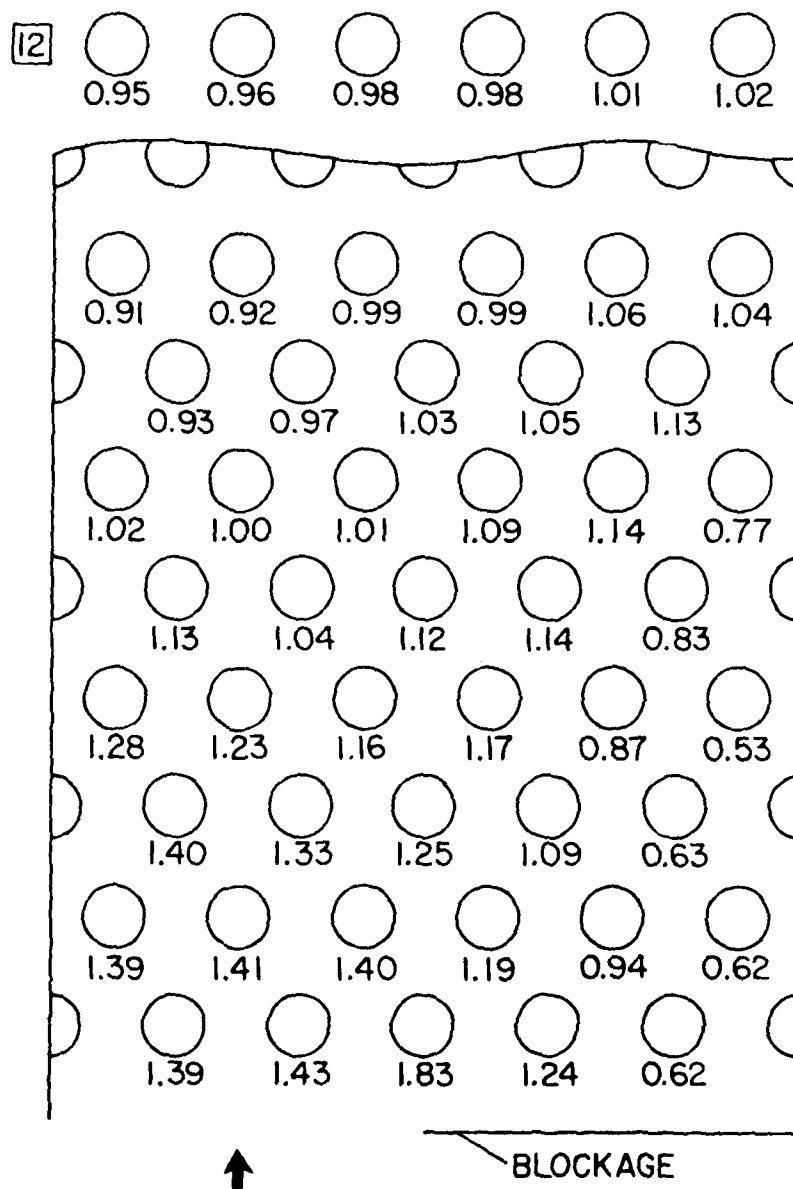


Fig. 6

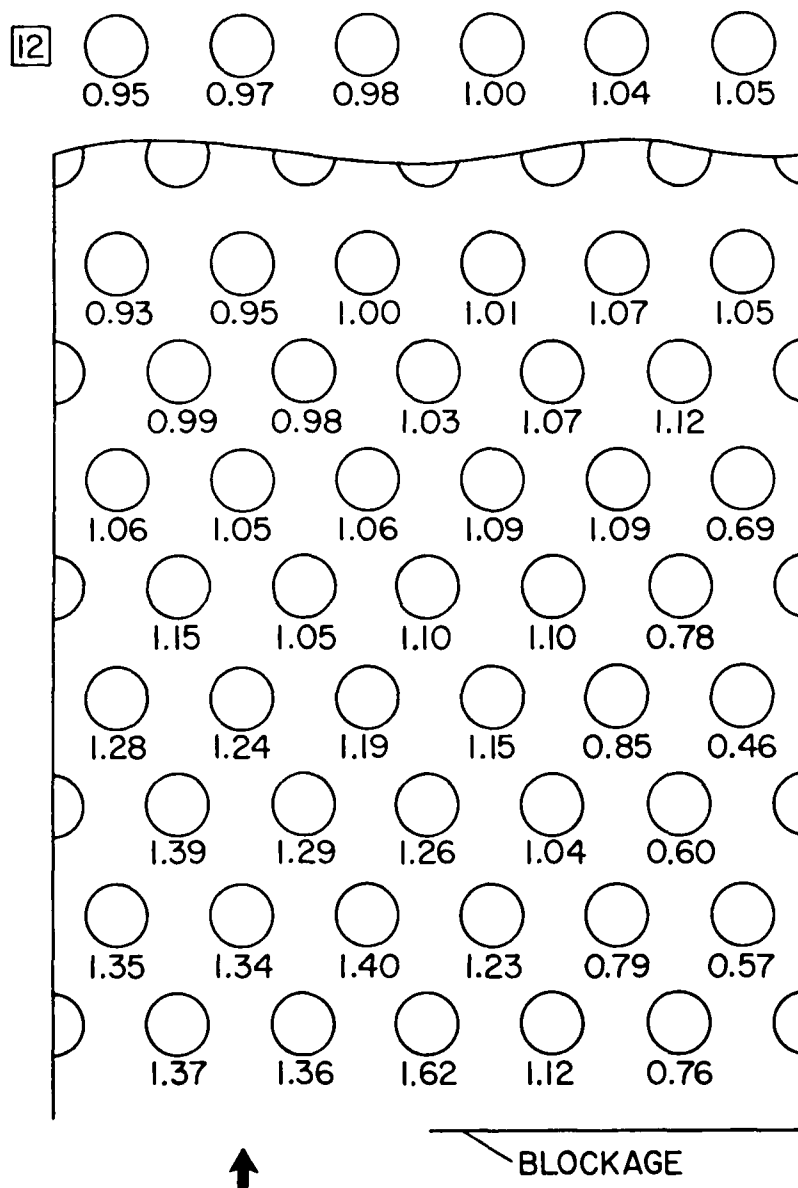


Fig. 7

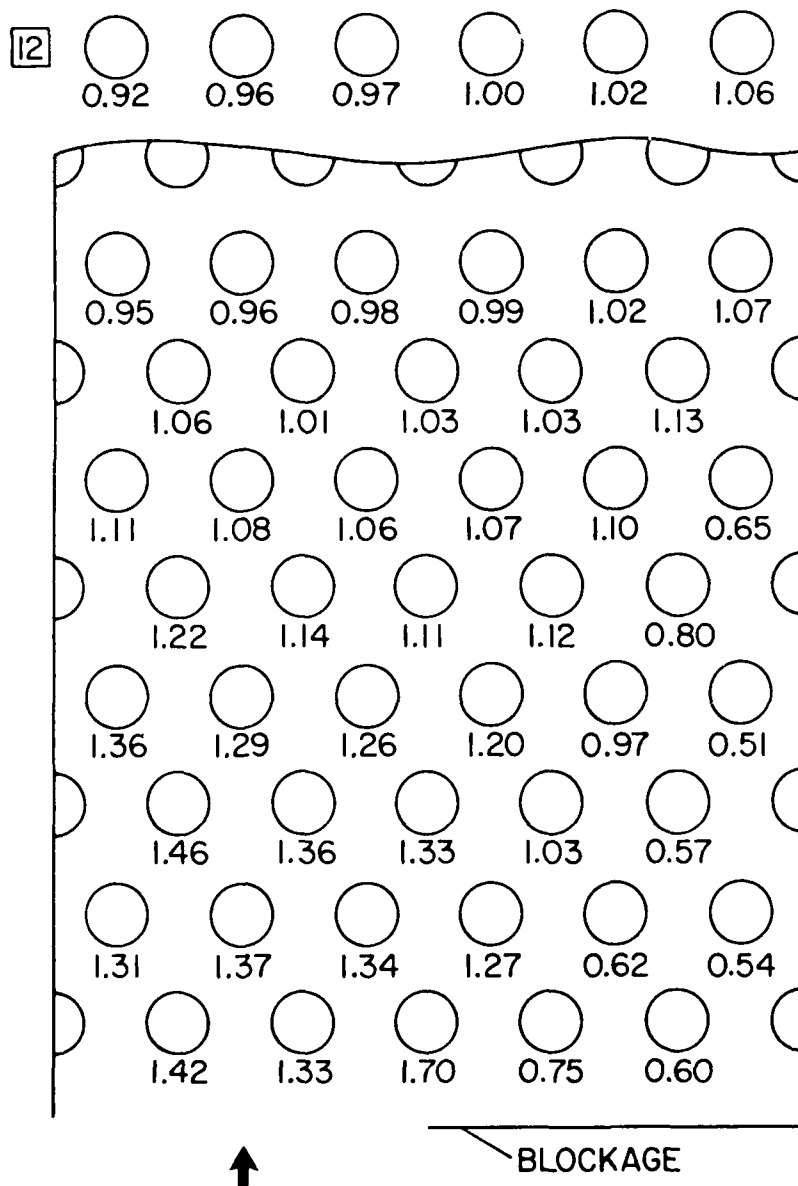


Fig. 8

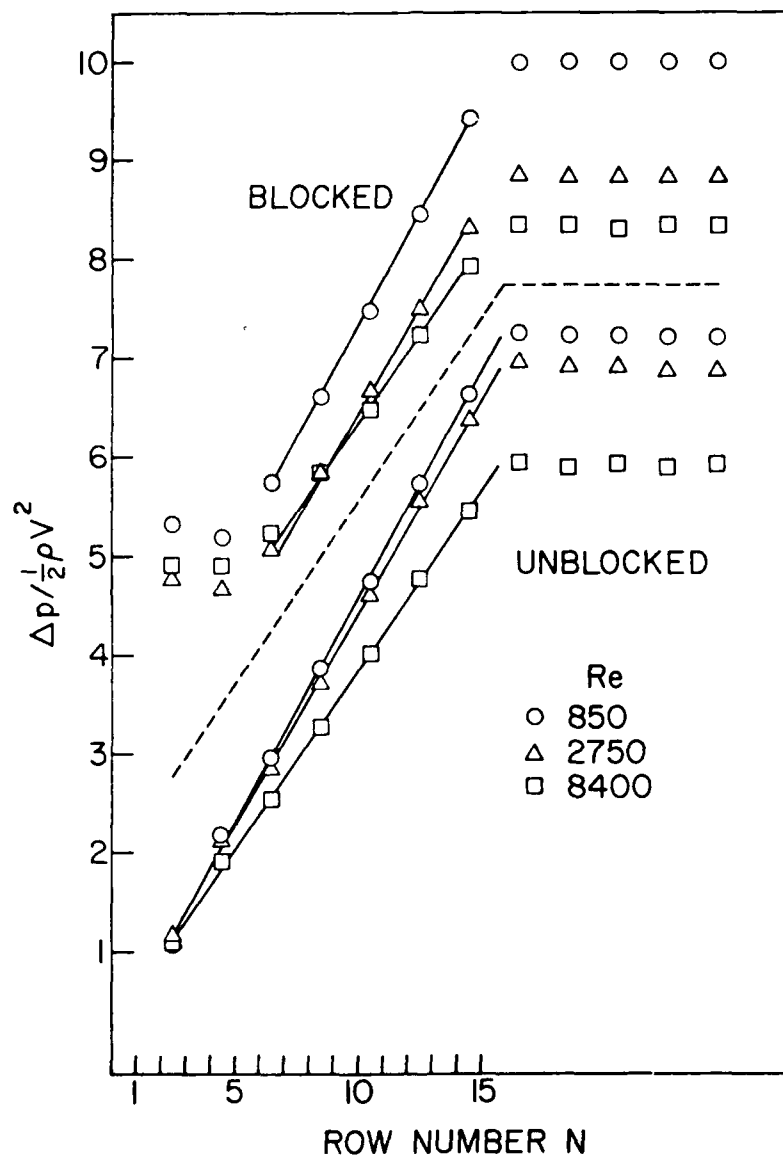


Fig. 9

Chapter 2

HEAT TRANSFER AND FLUID FLOW EXPERIMENTS WITH A TUBE
FED BY A PLENUM HAVING NONALIGNED INLET AND EXIT

ABSTRACT

Local turbulent heat transfer coefficients for airflow were measured in a tube situated downstream of a cylindrical plenum chamber in which the inflow was radial and the outflow was axial. Pressure drop measurements and flow visualization were performed to supplement the heat transfer experiments. The plenum length and diameter were varied systematically during the experiments, and the Reynolds number ranged from 10,000 to 60,000. Substantially higher Nusselt numbers in the tube were encountered for the present nonaligned plenum inlet/exit configuration than for a plenum with axially aligned inlet and exit or for an upstream hydrodynamic development section. For a given Reynolds number, the Nusselt numbers corresponding to the present plenum configuration were quite insensitive to the investigated geometrical parameters. The thermal development length was found to be substantially elongated due to swirl carried into the tube from the plenum; the presence of the swirl was confirmed by flow visualization. The net pressure loss due to the presence of the plenum was about 1.75 velocity heads and was quite insensitive to the geometrical parameters and to the Reynolds number.

NOMENCLATURE

c_p	specific heat of air
D	plenum chamber diameter
d	diameter of test section and development tubes
h	local circumferential-average heat transfer coefficient
K	dimensionless pressure loss coefficient, equation (5)
k	thermal conductivity of air
L_f	length of forward part of plenum

L_r	length of rearward part of plenum
\dot{m}	mass flow rate
Nu	local circumferential-average Nusselt number, hd/k
p	local static pressure
p_o	reference pressure
Δp_p	net plenum-related pressure loss, Fig. 2
Q_{cv}	convective heat transfer per control volume
q_x	convective heat flux
Re	Reynolds number, $4\dot{m}/\mu\pi d$
T_{bx}	bulk temperature at x
\bar{T}_{wx}	circumferential-average wall temperature at x
$T_{wx}(\theta)$	local circumferential temperature at x, θ
$\Delta T_{b,cv}$	bulk temperature rise per control volume
V^*	velocity at plenum inlet port
x	axial coordinate for test section
x'	axial coordinate for hydrodynamic development tube
θ	angular coordinate
μ	viscosity of air
ρ^*	density of air at plenum inlet port

INTRODUCTION

Fluid may be delivered to the tubes of a heat exchanger via a wide variety of plenum chamber geometries. Frequently, the fluid inlet to the plenum is not aligned with the fluid exit, so that the flow must turn as it passes through the plenum. The turning of the flow may induce a swirling motion which is carried into the tubes. In general, the nonaligned plenum inlet and exit will cause the flow which is fed to the tubes to be three dimensional, with transverse velocity components superposed on the axial mainflow. Despite the clear relevance to heat exchanger practice, it appears that a systematic study of heat transfer and pressure drop in the presence of a plenum with nonaligned inlet and exit has not yet appeared in the open literature.

In the experimental investigation to be reported here, a cylindrical plenum chamber is supplied with air through an inlet port that is transverse to the cylinder axis, so that the inflow is radial. The plenum exit, through which the air passes into a heated, instrumented tube, is axial. This configuration requires that the air turn as it passes through the plenum, thereby inducing the complex fluid flow phenomena that were discussed in the foregoing paragraph.

The research program encompassed three complementary sets of experiments, and two apparatuses were employed for its execution. In the main set of experiments, local heat transfer coefficients were measured along the length of the aforementioned electrically heated tube which is fed by the plenum discharge. For the most part, the heat transfer data were processed so as to yield circumferential average coefficients as a function of axial position along the tube. However, circumferential variations were also examined to identify the effect of swirl and fluid flow three dimensionality.

The second and third sets of experiments were devoted to fluid flow studies (without heat transfer). For these experiments, the heated test section was replaced with an unheated tube of identical bore diameter along which pressure taps were deployed. Pressure distributions were measured along both the tube which

supplies air to the plenum and the just-mentioned tube which receives the plenum discharge. These measurements enabled the determination of the net pressure loss due to the presence of the plenum, and these data will be presented in dimensionless form relative to the velocity head.

In the third set of experiments, the objective was to determine the patterns of fluid flow within the plenum. For this purpose, the oil-lampblack technique was employed. This technique is very well suited for revealing the flow pattern adjacent to a surface, as will be demonstrated via photographs to be presented later.

Geometrical parameters and airflow rate were varied during the course of the investigation. Two cylindrical plenums of different diameter were employed. Each of these plenums was designed to enable its axial length to be varied, and heat transfer data were collected for two plenum lengths for each. In the presentation of results, separate graphs are employed to portray the effects of the plenum length and diameter. For each of the plenum geometries for which heat transfer data were collected, the tube Reynolds number was varied from about 10,000 to 60,000. The pressure drop work was performed for four plenum lengths and spanned the same Reynolds number range as for the heat transfer.

As noted earlier, it does not appear that there is any published information on the effects of nonaligned plenum inlet and exit configurations, thereby eliminating the possibility of direct literature comparisons. To establish the effect of non-alignment, the present data will be compared with data corresponding to cylindrical plenums with aligned axial inlet and axial exit {1}. A further quantitative comparison is made with heat transfer results (also taken from {1}) for turbulent pipe flow without a plenum, where the heated tube is preceded by a hydrodynamic development length. Qualitative comparisons will be made with tube-flow heat transfer data in the presence of intentionally induced swirl {2,3}. The measured heat transfer coefficients in the far-downstream portion of the test section tube will be compared with those of the Petukhov-Popov correlation {4} for fully developed heat transfer.

THE EXPERIMENTS

Plenum chambers. A schematic diagram of the plenum chamber configuration that was employed in the experiments is presented in Fig. 1. The plenum is a cylinder of diameter D and length $(L_r + L_f)$, both internal dimensions. These dimensions were varied parametrically, as will be described shortly. Air was delivered to the plenum via a hydrodynamic development tube oriented so that the flow is radially inward at the inlet cross section. The plenum exit is a circular aperture centered in one of the end faces. Both the hydrodynamic development tube and the test section tube (which mates with the plenum exit) have the same internal diameter d which had a fixed value throughout the experiments.

The axial position of the plenum inlet port is specified by the lengths L_f and L_r , which respectively represent the distances between the centerline of the port and the front and rear faces of the plenum. Variation of L_r was accomplished by axial movement of the rear wall of the plenum.

Two positions of the rear wall were employed during the heat transfer experiments, respectively characterized by $L_r/d = 1$ and 5. The first of these corresponds to a minimal clearance between the inlet port and the rear wall so that, in effect, the entering fluid is denied the option of spreading rearward. The $L_r/d = 5$ rear-wall position was selected to match the $L_f/d = 5$ front-wall position that was built into the plenum. By this positioning, the entering fluid was given the option of spreading rearward (as well as forward), if that were its inclination. Thus, for the heat transfer studies, the employed variations of plenum length enabled evaluation of the effect of the presence or absence of an expansion space in the rear of the plenum, beyond the inlet port.

For the pressure drop studies, the same two values of L_r/D ($= 1$ and 5) were employed along with front-zone lengths L_f/d of 3 and 5. The $L_f/d = 3$ condition was obtained by implanting a disk of diameter D and length $= 2d$ into the forward-most portion of the plenum. A hole of diameter d bored along the axis of the disk mated

perfectly with the aperture in the front face of the plenum. With the disk in place, the forward-zone length available to the air was reduced from $L_f/d = 5$ to $L_f/d = 3$.

The use of an inserted disk to vary L_f/d in the heat transfer studies was considered and rejected. This is because such a disk would have created a hydrodynamic development length (equal to $2d$) upstream of the heated tube and might also have provided a path for extraneous heat conduction.

Two different plenum chamber diameters were employed, respectively $D/d = 3$ and 6 (actually, 2.96 and 5.91).

Both plenums were made of plexiglass, with the exception of the front face, as will be described shortly. The movable rear wall consisted of a disk fitted with a handle-like rod, as seen in Fig. 1. An air-tight seal between the plenum wall and the contacting edge of the disk was achieved with a pair of O-rings. Once moved to a desired axial position, the disk could be locked in place.

The plenum inlet port consisted of a bored hole which passed radially through the cylindrical wall of the plenum and through a contoured plexiglass boss that had been affixed to the outside of the wall to provide added thickness. The bored hole was recessed in such a way that there was no discontinuity in the flow cross section as the hydrodynamic development tube mated with the plenum inlet port.

For the pressure drop studies, the front wall of the plenum was a plexiglass disk with a centered aperture sized to accommodate the outer diameter of the pressure test section. In the heat transfer experiments, the plenum front wall was part of the defense devised to avoid extraneous heat losses. In the case of the smaller diameter plenum, the entire front wall consisted of an annular disk made of 0.043 cm (0.017 in.) thick fiberglass circuitboard. For the larger diameter plenum, the fiberglass disk was framed by a plexiglass annulus.

The inner diameter of the fiberglass disk was made identical to the outer diameter of the test section tube, so that the disk could just slip over the tube. When assembled, the upstream faces of the disk and tube lay in a continuous plane.

The only thermal path between disk and tube was through their 0.043 cm (0.017 in.) interface. This minimal contact, taken together with the low conductivity of the fiberglass, created a strong blockage of extraneous heat conduction. Possible air leaks were sealed with a fillet of silicone rubber applied just downstream of the fiberglass disk and by the use of pressure-sensitive tape at strategic locations.

Heated test section. The test section was a stainless steel tube with an internal diameter (after honing) of 2.362 cm (0.930 in.), a wall thickness of 0.089 cm (0.035 in.), and a heated length of about seventy diameters. Heating was accomplished by the passage of voltage-stabilized a.c. electric current through the tube wall. To facilitate the heating, copper rings were soldered to the tube at its upstream and downstream ends. Current was conveyed to (or from) the respective rings by six rod-like copper conductors.

The copper rods situated at the upstream end of the tube were each fitted with a differential thermocouple to detect possible extraneous heat conduction. To null out the extraneous conduction, a guard heating/cooling arrangement was devised which enabled the readings of the differential thermocouples to be reduced to zero. It was not thought necessary to use a similar arrangement at the downstream-end current conductors because data were not collected in that immediate neighborhood.

As a further defense against extraneous losses, the test section tube was suspended by monofilament nylon lines rather than being supported by rigid structural members. In addition, the test section, the plenum, and a mixing box positioned downstream of the test section were situated within an insulation enclosure. The enclosure consisted of a plywood box whose inner walls were lined with polystyrene sheet insulation. Silica aerogel powder with a thermal conductivity fifteen percent less than that of air filled the core of the enclosure.

The test section tube was instrumented with 30-gage, specially calibrated copper-constantan thermocouples spot welded to its outer surface. The thermocouples were oriented so that the leads lay along the expected isothermal directions. In the first eight diameters of the tube, thermocouples were installed at twelve

axial stations, and each such station was equipped with four thermocouples affixed 90 deg apart. The subsequent fifteen measurement stations were each equipped with two thermocouples.

Other components and instrumentation. To identify the other system components, it is convenient to follow the flow path of the air. The system was operated in the open-circuit mode, with air being supplied from a dryer-equipped regulated central compressor. After passing through a valve, regulator, and filter, the air was ducted to a settling chamber whose discharge was fed into the 65-diameters-long hydrodynamic development pipe. The settling chamber served to uncouple the airflow from its previous history, while the hydrodynamic development tube provided a well-defined velocity distribution at the plenum inlet. The air then passed through the plenum and the test section (as noted earlier, different test sections were used for the heat transfer and fluid flow experiments). At the test section exit, in the case of the heat transfer experiments, the air was mixed in a multiple-baffle mixing box. In both sets of experiments, the last component of the flow circuit was a rotameter which measured the volume flow. Two rotameters, both specifically calibrated, were employed to cover the investigated Reynolds number range (10,000 to 60,000).

The test section thermocouples have already been mentioned. In addition, two thermocouples threaded through the wall of the plenum served to measure the inlet bulk temperature of the air. A pair of thermocouples were also positioned in the mixing box at the downstream end of the test section. All thermocouples were read and recorded by a Fluke 2240B scanning, programmable datalogger having a 1 μ V resolution.

For the pressure drop studies, the signals from the various taps were conveyed via plastic tubing to a selector switch, the output of which was sensed by a Baratron capacitance type, solid-state pressure meter capable of resolving 10^{-4} Torr.

Flow visualization. The oil-lampblack technique was employed to facilitate visualization of the pattern of fluid flow adjacent to the walls of the plenum

chamber. To enable a permanent record of the visualized flow patterns to be obtained, white, plasticized contact paper was applied to each portion of the plenum wall at which the flow was to be examined. A mixture of oil and lampblack powder, whose fluidity could be varied by using various oils and also by adding different proportions of lampblack to the oils, was applied to the surface of the contact paper. The mixture was either brushed on so that it covered a selected area of the surface or else was applied as a series of dots.

Under the action of the stresses exerted by the airflow, the mixture moved along the surface, and by doing so it revealed the direction of the flow adjacent to the surface. Once the visualization pattern had been established, the contact paper was removed from the plenum wall and placed flat on a cardboard backing. In this way, the visualization pattern was available for careful study and for photography.

Entry to the plenum chamber for installation and removal of the contact paper was via the movable end wall, which could be detached from the rest of the plenum. The installation and removal procedure required that a hand be inserted into the plenum. This was possible only for the larger of the two plenum diameters (i.e., $D/d = 6$), so that the visualization studies were confined to that plenum.

Visualization runs were attempted over the same range of Reynolds numbers as for the heat transfer experiments, but crisply defined flow pattern traces could be obtained only at the higher Reynolds numbers. This is because the shear stresses associated with the lower Reynolds number flows were too weak to move the oil-lampblack mixture (for these Reynolds numbers, the fluidity of the mixture was made as low as possible consistent with the avoidance of sagging).

DATA REDUCTION

Heat transfer coefficients. The main focus of the data reduction was the evaluation of local heat transfer coefficients at each of the instrumented cross sections along the heated test section tube. The coefficients to be obtained are circumferential average values; however, as will be demonstrated later, even the largest circumferential variations were modest and were confined to the first few diameters downstream of the tube inlet.

The ingredients needed to evaluate the local coefficient are the convective heat transfer rate per unit surface area, the inside wall temperature, and the bulk temperature--all local quantities. The experimental data available for the determination of these quantities are the measured wall temperatures (on the outside of the tube) and the power input to the test section. It is readily shown by calculation that the temperature difference across the tube wall is negligible (actually, the same order as the resolving power of the instrumentation). Thus, the inside wall temperatures were obtained from the measured outside wall temperatures. At any axial station x , the wall temperature was taken as the average of the circumferential temperature measurements and will, correspondingly, be denoted as \bar{T}_{wx} .

The procedure for determining the local heat flux and local bulk temperature will now be described. For the heat flux determination, the tube wall is subdivided into a succession of axial segments of length $\Delta x_1, \Delta x_2, \dots$. The axial boundaries of each segment are positioned midway between the neighboring temperature measurement stations. Each of these segments is used as a control volume for a heat balance. For each control volume, the following energy transfers are considered:

1. Internal heat generation, which is determined by prorating the power input to the test section as a whole
2. Axial heat conduction entering the control volume at its downstream face

3. Axial heat conduction leaving the control volume at its upstream face
4. Heat loss from the outer cylindrical surface of the control volume through the insulation and into the ambient air
5. Convective heat transfer from the inner cylindrical surface of the control volume to the airflow in the tube

The axial heat conduction terms (items 2 and 3) were evaluated from the measured wall temperatures with the aid of a central-difference form of Fourier's law. Item 4, the calculated heat loss through the insulation, was based on a conduction shape factor for the insulation enclosure that had previously been obtained from a finite difference solution.

From the foregoing, it is seen that all terms of the energy balance except the convective heat transfer (item 5) were evaluable from the experimental data, thereby enabling its determination. The convective heat transfer for each control volume was divided by the corresponding convective surface area, yielding the heat flux q_x , where x is the coordinate of the temperature measurement station contained within the control volume.

The determination of the bulk temperature T_{bx} at x will now be described. For a fluid control volume which has the same axial boundaries as the tube-wall control volume, the bulk temperature rise of the air is

$$\Delta T_{b,cv} = Q_{cv} / \dot{m} c_p \quad (1)$$

where Q_{cv} is the convective heat transfer for the control volume (already evaluated as described in the preceding paragraph), and \dot{m} and c_p respectively denote the mass flow rate and the specific heat. Repetitive application of equation (1) to the successive control volumes, starting with the measured inlet bulk temperature T_{b1} , yields the bulk temperature at all of the axial boundaries of the control volumes. Then, for an axial station x within any given control volume, T_{bx} was obtained by linear interpolation between the bulk temperatures at the boundaries.

From the computations described in the foregoing, the local (circumferential average) heat transfer coefficient was obtained from

$$h = q_x / (\bar{T}_{wx} - T_{bx}) \quad (2)$$

which was then made dimensionless via the local Nusselt number

$$Nu = hd/k \quad (3)$$

The thermal conductivity appearing in equation (3) was based on the local bulk temperature.

The Nusselt number results are parameterized by the Reynolds number defined in the conventional manner for pipe flows

$$Re = 4\dot{m}/\mu\pi d \quad (4)$$

where μ is the viscosity corresponding to the mean bulk temperature of the air.

Plenum-related pressure loss. Attention is now turned to the net pressure loss due to the presence of the plenum, which is illustrated in Fig. 2. Although the figure corresponds to a specific case ($D/d = 6$, $L_f/d = L_r/d = 5$, $Re = 27,900$), the character of the pressure distribution shown there pertains to all of the cases for which data were collected. A schematic diagram at the upper right of the figure shows the setup for the pressure measurements and identifies the coordinates x and x' which respectively correspond to axial stations in the test section tube and in the hydrodynamic development tube. In the main part of the figure, p vs x' for the development tube is plotted at the left and p vs x for the test section is plotted at the right.

The pressure distribution in the development tube is seen to be linear, and a linear distribution having the same slope exists in the downstream portion of the test section. In the figure, the straight lines that pass through the data are least-squares fits. The p vs x' line for the development tube has been extrapolated downstream to the plenum inlet, while the p vs x line for the test section has been extrapolated upstream to the plenum exit. These extrapolations are shown as dashed lines in the figure. Had the plenum not been present, these

lines would have been colinear. With the plenum in place, there is a vertical offset between the lines which is denoted by Δp_p , as illustrated in the figure.

The quantity Δp_p is the net plenum-related pressure loss. It will be presented in terms of a dimensionless loss coefficient K defined as

$$K = \Delta p_p / (\frac{1}{2} \rho V^2)^* \quad (5)$$

The denominator of equation (5) is the velocity head corresponding to the density ρ^* of the air in the tube at the inlet of the plenum, so that

$$(\rho V^2)^* = \dot{m}^2 / \rho^* (\pi d^2 / 4)^2 \quad (6)$$

RESULTS AND DISCUSSION

The presentation of results will begin with the flow visualization and then, in succession, goes on to heat transfer and pressure drop.

Flow visualization. Of the various flow characteristics that were revealed by the visualization studies, two were thought to be of particular interest and will be described with the aid of photographs. The first has to do with the issue of whether any significant portion of the fluid which enters the plenum streams into the rear part of the chamber or whether, alternatively, the flow heads directly for the exit aperture in the front face and ignores the rear zone. Evidence of a very strong flow into the rear zone is provided by Fig. 3, for which $D/d = 6$, $L_f/d = L_r/d = 5$, $Re \sim 60,000$. The region illustrated in the figure extends from the rear wall to the front wall of the plenum (the rear wall is at the left margin of the photo and the front wall is at the right margin) and subtends a 180 deg arc on the cylindrical wall which faces the incoming flow. The flow pattern was obtained by applying the oil-lampblack mixture to a five-cm square on the plenum wall just opposite the fluid inlet port.

It can be seen from the figure that after impinging on the wall, the air moves in all directions, but most of the flow is in the axial direction, either backward toward the rear wall of the plenum or forward toward the front wall. The strong backflow along the wall is quite remarkable. Since this backflowing fluid

must eventually exit the plenum through the aperture in its front wall, it must turn (presumably at the very rear of the plenum) and then become a forward flowing axial stream.

The absence of a rear-zone expansion space (small L_r/d) eliminates the strong backflow shown in Fig. 3 and, by this, profoundly effects the pattern of fluid flow in the plenum. It would not be surprising, therefore, if the flow presented to the tube by the plenum were to be quite different for small L_r/d and large L_r/d . This matter will be revisited when the heat transfer results are presented.

The curling of the flow lines adjacent to the left and right margins of the photograph corresponds to the turning of the flow as it responds to the blocking action of the front and rear walls. Aside from the turning, strong circumferential motions are not in evidence.

The presence of circumferential motions near the end walls suggests the possibility that fluid passing from the plenum into the test section may carry with it a swirl. This is confirmed by the photograph presented in Fig. 4, which corresponds to $D/d = 6$, $L_f/d = 5$, $L_r/d = 1$, $Re \sim 60,000$. The flow pattern was obtained by applying the oil-lampblack mixture in the form of a 180 deg arc on the front face of the plenum. As is evident from the figure, the flow lines emanating from the arc are not radial but curved, indicating the existence of a swirling flow near the exit of the plenum (i.e., at the inlet of the test section). Swirl was also observed for the longer plenum ($L_f/d = L_r/d = 5$), but the flow lines were less sharply etched than those of Fig. 4. It may be expected that the swirl will affect the heat transfer in the test section.

Heat transfer results. The first set of heat transfer results to be presented is aimed at identifying the effects of the upstream fluid-flow geometry on the local Nusselt number distribution for turbulent heat transfer in a tube, and Fig. 5 has been prepared for this purpose. The figure consists of two graphs, respectively for $Re = 10,700$ and $Re = 50,000$. In each graph, the local Nusselt number is

plotted as a function of the dimensionless axial coordinate x/d .

As illustrated schematically in the right-hand graph, the results for three different configurations are compared. The solid line corresponds to the present nonaligned inlet/exit plenum configuration, and the short-dashed lines are for a plenum with axially aligned inlet and exit. The third line (long dashes) depicts the results for a very short plenum so that, in effect, they correspond to the case of heat transfer in a tube preceded by an unheated hydrodynamic development section of the same diameter. Both comparison cases were taken from {1}. Although all of the results of Fig. 1 are experimental, the data points have been omitted to obtain greater clarity (the actual data for the present experiments will be reported shortly).

The present results shown in Fig. 5 are for $D/d = 3$, $L_f/d = 5$, $L_r/d = 1$, while those for the aligned inlet-exit configuration are for the same D/d and for a plenum length equal to $5d$ (the closest length-diameter ratio available for the comparison). Although the plotted results pertain to the aforementioned geometrical parameters, it is important to note that graphs which are both qualitatively and quantitatively similar to Fig. 5 would be obtained if the results for the other investigated geometrical parameters had been plotted.

Inspection of Fig. 5 shows that there is a definite ordering of the local Nusselt numbers with upstream fluid-flow geometry. Those for the nonaligned plenum inlet/exit are the highest, followed by those for the aligned plenum inlet/exit. The lowest Nusselt numbers are those for the no-plenum case. As is to be expected, the greatest spread among the three sets of results occurs in the immediate neighborhood of the inlet, with decreasing deviations with increasing downstream distance. At $x/d = 2.5$, the overall spread in the results is about 35 percent. By $x/d = 10$, the overall spread has dropped to just below 5 percent for $Re = 10,700$ but is still slightly in excess of 15 percent for $Re = 50,000$. Even at $x/d = 30$, there is still a 10 percent enhancement in evidence for the latter Reynolds number.

The just-discussed ordering of the curves in Fig. 5 is consistent with physical expectation. In particular, the nonaligned plenum inlet/exit yields a more agitated flow, supplemented by swirl, than do the other configurations. The aligned plenum inlet/exit presents a non-fully-developed flow to the test section, thereby giving rise to higher coefficients than does the already developed flow.

Attention will now be turned to a detailed presentation of the Nusselt number results. The presentation will be made in two distinct formats--the first aimed at identifying the effect of the plenum rear-zone expansion space L_r/d and the second at identifying the effect of plenum diameter D/d .

In Figs. 6 and 7, the local Nusselt number data are plotted as a function of x/d for five Reynolds numbers between 10,700 and 59,000, with the two lower Re presented in Fig. 6 and the three upper Re in Fig. 7. Each of these figures shows results for $D/d = 3$ and 6 on respective axes that are displaced both vertically and horizontally, so that the $D/d = 3$ data are referred to the left ordinate and lower abscissa while the $D/d = 6$ data are referred to the right ordinate and upper abscissa.

The main concern of these figures is with the size of the plenum rear-zone expansion space, and data for $L_r/d = 1$ and $L_r/d = 5$, respectively denoted by circle and square symbols, are plotted to examine this matter. Inspection of Figs. 6 and 7 reveals a remarkable insensitivity of the results to L_r/d in the range investigated. The greatest deviations in the Nusselt numbers for the two L_r/d are in the 3 - 4 percent range, and these tend more to occur at the higher Re values. The insensitivity to L_r/d is in evidence for both $D/d = 3$ and 6, with the results for the latter being virtually independent of L_r/d . This finding is remarkable in light of the expectations discussed in connection with the flow visualization. It may, perhaps, be due to a washing out of various specifics of the plenum flow field when the fluid is caused to sharply contract as it exits the plenum and enters the test section.

There are various other aspects of Figs. 6 and 7 which are worthy of discussion. The respective Nusselt number distributions display what appears to be a classical developmental pattern, starting with very high values at the inlet and decreasing monotonically with increasing downstream distance. The absence of evidence of flow separation at the sharp-edged inlet may, at first thought, seem somewhat surprising. However, in other experiments at Minnesota, unrelated to the present work, it was found that the separated flow reattaches upstream of $x/d = 1$. Since $x/d = 1$ is the first measurement station in the present apparatus, the possible flow separation could not be detected.

Another point worthy of mention is the persistence of a slow dropoff of the distributions in the far downstream portion of the tube. Indeed, fully developed conditions appear not to have been attained even at $x/d = 58$, the last measurement station. This behavior is believed due to the swirl which was carried into the test section tube from the plenum.

In this regard, the literature was examined and corroborating information encountered. Blum and Oliver {2} also obtained heat transfer coefficients which continued to drop off beyond the tube length at which fully developed turbulent heat transfer coefficients are normally obtained. In their investigation, swirl was generated by tangential injection of air near the entrance of a heated tube. By extrapolating the measured axial distributions of the heat transfer coefficient beyond the region of measurement, they estimated that about 100 diameters (from the inlet) would be required to obtain fully developed conditions at $Re = 50,000$. For a Reynolds number of approximately 7000, a 75-diameter estimate was made. The elongated development length for swirl-flow heat transfer was confirmed by Hay and West {3}. They found that the heat transfer coefficients at eighteen diameters from the pipe inlet (their last measuring station) were continuing the decrease that marks the thermal entrance region.

The data of Figs. 6 and 7 affirm the expected increase of the Nusselt number

with Reynolds number at all axial stations. The Nusselt numbers at the downstream end of the tube will shortly be compared to literature correlations for fully developed heat transfer conditions.

Although Figs. 6 and 7 indicate a qualitatively similar behavior of the results for $D/d = 3$ and 6, these figures do not lend themselves to a quantitative comparison of the effect of D/d . To facilitate such a quantitative comparison, Figs. 8 and 9 have been prepared. Figures 8 and 9 are similar in structure to Figs. 6 and 7, but with the difference that results for different D/d are compared for a given L_r/d (in Figs. 6 and 7, results for different L_r/d are compared for a given D/d). Figure 8 conveys results for $Re = 10,700$ and $15,200$, while results for $Re = 24,400$, $39,300$, and $59,000$ are presented in Fig. 9. In each figure, the results for $L_r/d = 1$ and 5 are plotted on displaced axes to preserve clarity. The data points have been omitted from these figures because the actual data have already been presented in Figs. 6 and 7.

Examination of Figs. 8 and 9 shows that the effect of D/d is modest. For the most part, the spread between the curves for the two D/d values is no more than four percent, and there is only one case ($L_r/d = 1$, $Re = 24,400$) where a six percent spread is encountered. It appears that plenums with a smaller rear-zone expansion space (i.e., smaller L_r/d) are slightly more sensitive to D/d than are plenums with a larger expansion space.

When taken together, Figs. 6 - 9 indicate a general insensitivity of the local Nusselt number results to the plenum geometrical parameters that were investigated. Thus, the results presented here are of a universal character.

Although thermally developed conditions were not strictly attained in the far downstream portion of the tube, it is evident from the foregoing figures that fully developed Nusselt numbers were being approached. In this regard, it is interesting to compare the measured coefficients at the last axial station ($x/d = 58$) with the well-established Petukhov-Popov equation (4) for fully developed

heat transfer. The comparison shows that the present data deviate by no more than six percent from the Petukhov-Popov equation, which is its purported accuracy.

As a final matter in the presentation of the heat transfer results, brief consideration will be given to the circumferential variations induced by the non-aligned plenum inlet and exit. The nonalignment causes circumferential nonuniformities in the velocity entering the test section.

A presentation of the extreme circumferential variations encountered in all of the investigated cases is shown in Fig. 10. This figure contains a succession of graphs, each for a given x/d ranging from 0.5 to 3.5. In each graph, the measured circumferential wall-temperature distribution is plotted as a function of the angle θ . The temperature distribution is presented in dimensionless form, with $(T_{wx}(\theta) - T_{bx})$ as the numerator and $(\bar{T}_{wx} - T_{bx})$ as the denominator. For purposes of orientation, θ values between 180 and 360 deg are on the side of the tube opposite the plenum inlet port, while angles between 0 and 180 deg are on the same side as the inlet port. The results shown in Fig. 10 are for $D/d = 6$, $L_f/d = 5$, $L_r/d = 1$, and $Re = 59,000$.

From Fig. 10, it is seen that the circumferential temperature distribution is nearly sinusoidal, with a maximum at $\theta = 90$ deg and a minimum at $\theta = 270$ deg. Since the flow entering the tube is expected to be concentrated on the side opposite the plenum inlet port, the temperature minimum at $\theta = 270$ deg is altogether reasonable, as is the maximum at $\theta = 90$ deg.

The amplitude of the variation (relative to the mean) is about ten percent at the first two measurement stations, whereafter it decreases such that at $x/d = 3.5$ temperature uniformity is nearly established. It should be emphasized that these are the largest amplitudes that were encountered. Thus, it can be concluded that circumferential variations are moderate and do not merit special consideration for most applications.

Plenum-related pressure losses. The net plenum-related pressure loss Δp_p

was illustrated in Fig. 2, and its dimensionless counterpart K was defined in equation (5). For a fixed plenum geometry, K was found to be relatively insensitive to the Reynolds number, with typical variations being ± 3 percent about the mean. This behavior indicates that inertial losses dominate over friction losses.

The mean value of K for each of the investigated geometrical configurations is listed in Table 1. The range of K is seen to be markedly narrow--between 1.66 and 1.86, and there are no consistent trends with the geometrical parameters. An overall average is 1.75, and this value may be suitable for most design purposes. In round numbers, the mean K value for the present nonaligned plenum inlet/exit configuration exceeds that for an axially aligned inlet/exit configuration (1) by about one.

CONCLUDING REMARKS

The present investigation appears to be the first systematic experimental study of the effect of a nonaligned plenum inlet/exit configuration on the turbulent heat transfer characteristics of a tube fed by the plenum. Pressure drop measurements and flow visualization were performed to supplement the heat transfer experiments. The plenum used in the experiments was a cylinder with a radial inlet and an axial exit.

The flow visualization showed that when there is an expansion space in the plenum to the rear of the inlet port, the entering fluid tends to stream into that space before turning and heading toward the exit in the front face of the plenum. The presence of swirl in the flow entering the test section tube was also confirmed by the visualization.

The perturbed, nonaxisymmetric flow induced in the plenum by the nonaligned inlet and exit gives rise to enhanced heat transfer in the test section. Enhancement was identified by comparisons with results for a tube fed either by a plenum with axially aligned inlet and exit or by an unheated hydrodynamic development tube having a diameter equal to that of the test section. The extent of the enhancement is greater at higher Reynolds numbers.

The distribution of the local Nusselt number along the length of the test section at a given Reynolds number was found to be quite insensitive to the investigated geometrical parameters--the size of the plenum rear-zone expansion space and the plenum diameter. The distribution curves did not show evidence of flow separation at the inlet, but separation might have occurred upstream of the first measurement station ($x/d = 1$). A slow dropoff of the curves persisted even in the far downstream portion of the tube. The elongated thermal development length is due to the swirl that was carried into the test section from the plenum. The Nusselt numbers at the last measurement station agreed well with those from the Petukhov-Popov equation.

Circumferential temperature variations induced by the nonaxisymmetric flow entering the test section tube were moderate and were confined to the immediate neighborhood of the inlet.

The net pressure loss induced by the plenum, nondimensionalized by the velocity head, was relatively insensitive to both the Reynolds number and the geometrical parameters. The mean value of the pressure loss is 1.75 velocity heads.

REFERENCES

1. Lau, S. C., "Effect of Plenum Length and Diameter on Turbulent Heat Transfer in a Downstream Tube and on Plenum-Related Pressure Losses," Journal of Heat Transfer, Vol. 103, 1981, pp. 415-422.
2. Blum, H. A. and Oliver, L. R., "Heat Transfer in a Decaying Vortex System," ASME paper 66-WA/HT-62, 1966.
3. Hay, N. and West, P. D., "Heat Transfer in Free Swirling Flow in a Pipe," Journal of Heat Transfer, Vol. 97, 1975, pp. 411-416.

Table 1
Pressure Loss Coefficient K

L_f/d	L_r/d	D/d	
		3	6
3	1	1.83	1.68
3	5	1.86	1.73
5	1	1.68	1.79
5	5	1.75	1.66

4. Petukhov, B. S., "Heat Transfer and Friction in Turbulent Flow with Variable Physical Properties," in Advances in Heat Transfer, Vol. 6, 1970, pp. 503-564.

FIGURE CAPTIONS

- Fig. 1 Plenum chamber configuration used in the experiments
- Fig. 2 Illustration of the determination of the net plenum-related pressure loss Δp_p . The data correspond to $D/d = 6$, $L_f/d = L_r/d = 5$, $Re = 27,900$.
- Fig. 3 Fluid flow pattern along the cylindrical wall of the plenum which faces the inlet port
- Fig. 4 Fluid flow pattern showing the presence of swirl at the plenum exit
- Fig. 5 Comparison of Nusselt number distributions corresponding to various upstream fluid-flow geometries
- Fig. 6 Nusselt number distributions showing the effect of the size of the plenum rear-zone expansion space L_r/d , $Re = 10,700$ and $15,200$
- Fig. 7 Nusselt number distributions showing the effect of the size of the plenum rear-zone expansion space L_r/d , $Re = 24,400$, $39,300$, and $59,000$
- Fig. 8 Nusselt number distributions showing the effect of the plenum diameter D/d , $Re = 10,700$ and $15,200$
- Fig. 9 Nusselt number distributions showing the effect of the plenum diameter D/d , $Re = 24,400$, $39,300$, and $59,000$
- Fig. 10 Circumferential wall temperature distributions showing the largest variations encountered in all of the investigated cases

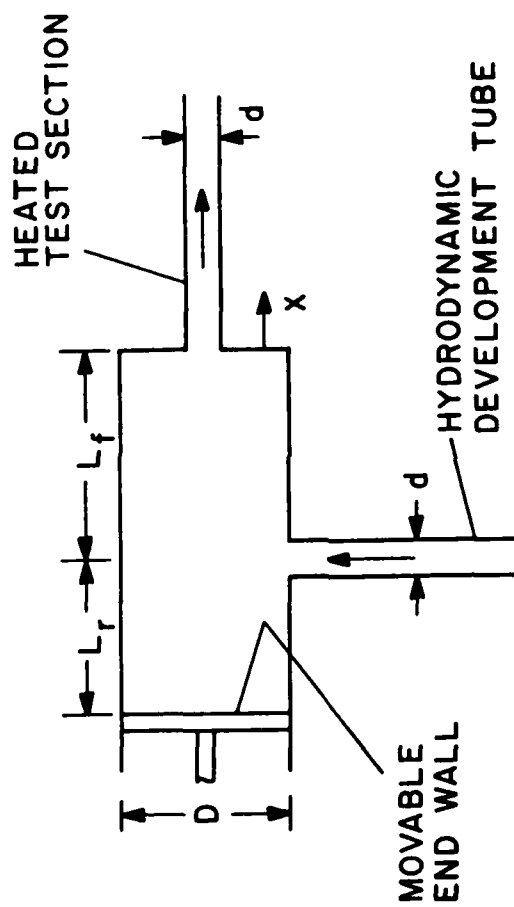


Fig. 1

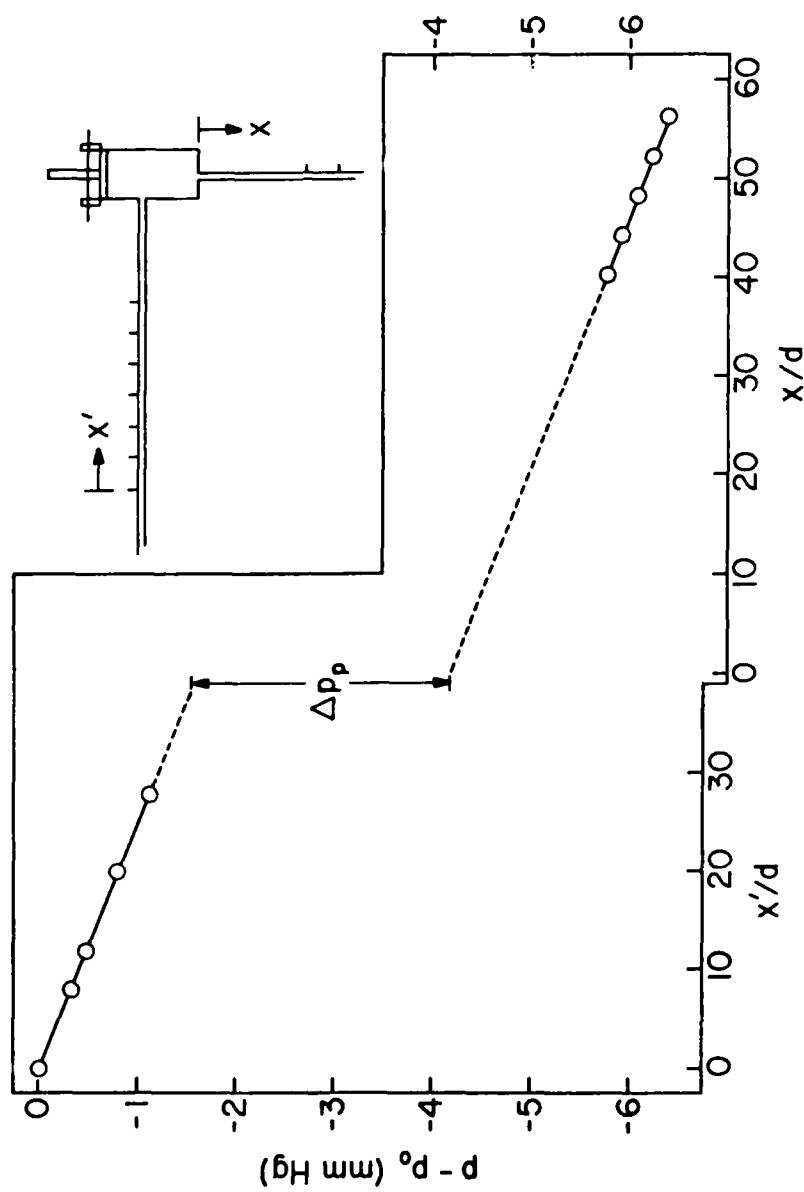


Fig. 2

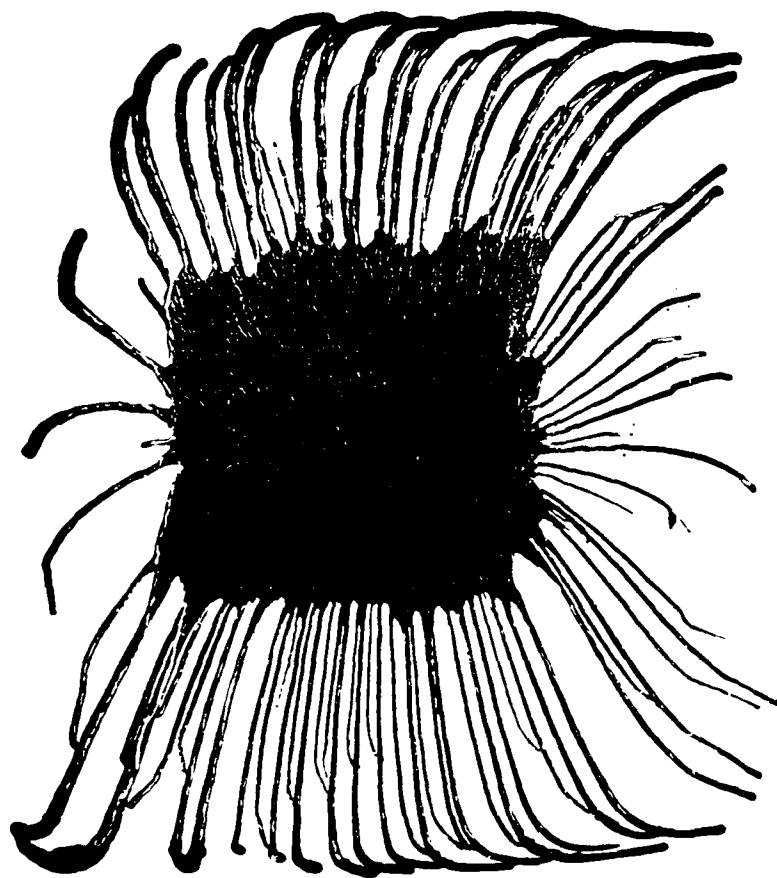


Fig. 3

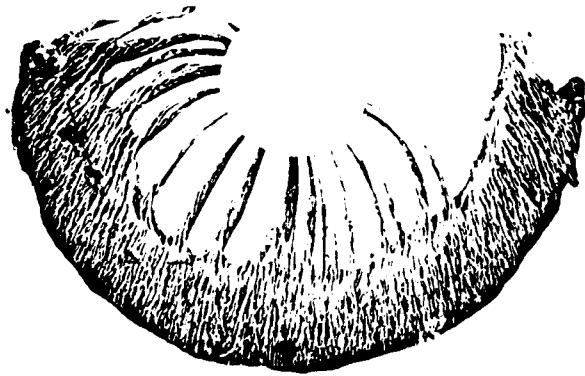


Fig. 4

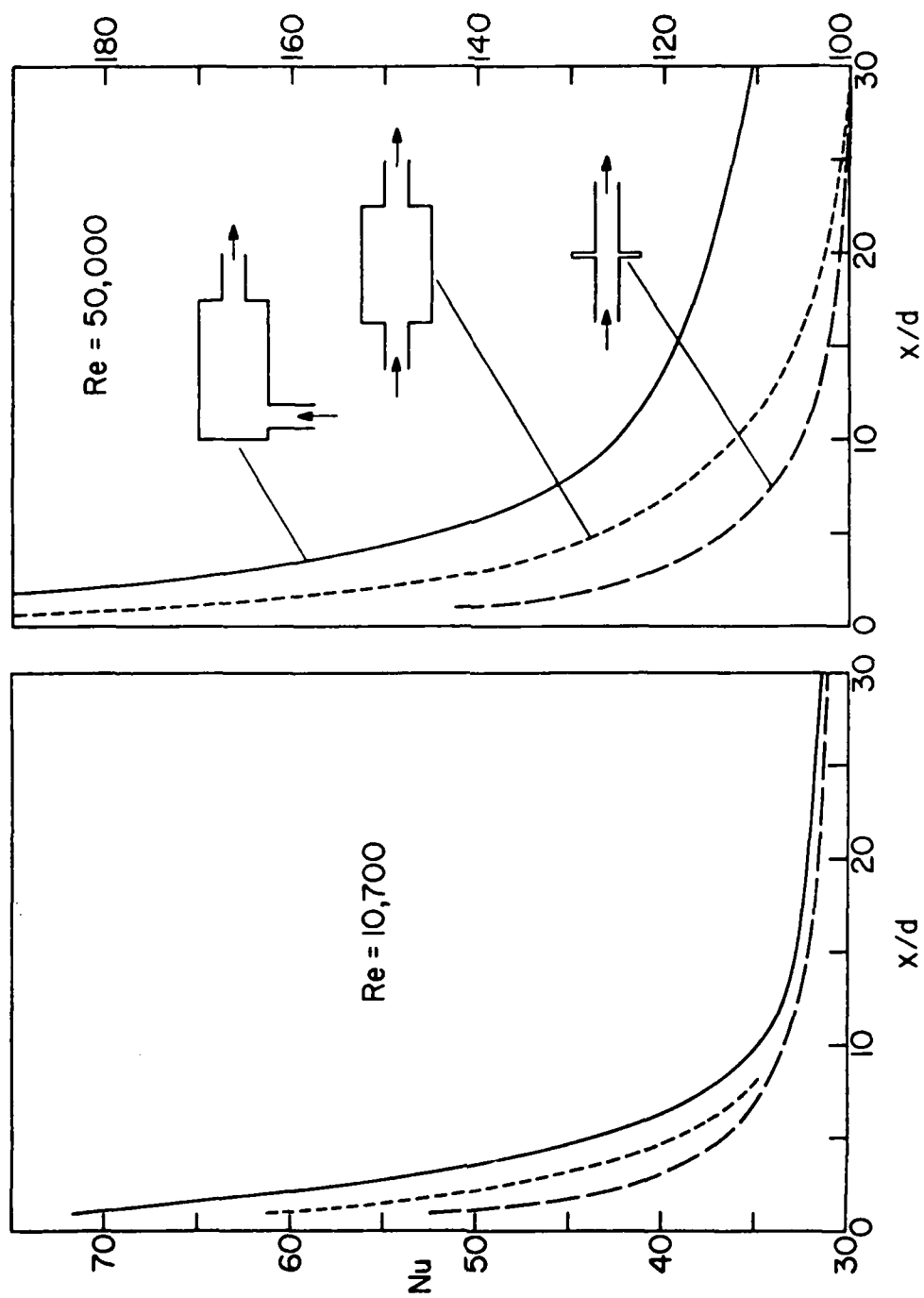


Fig. 5

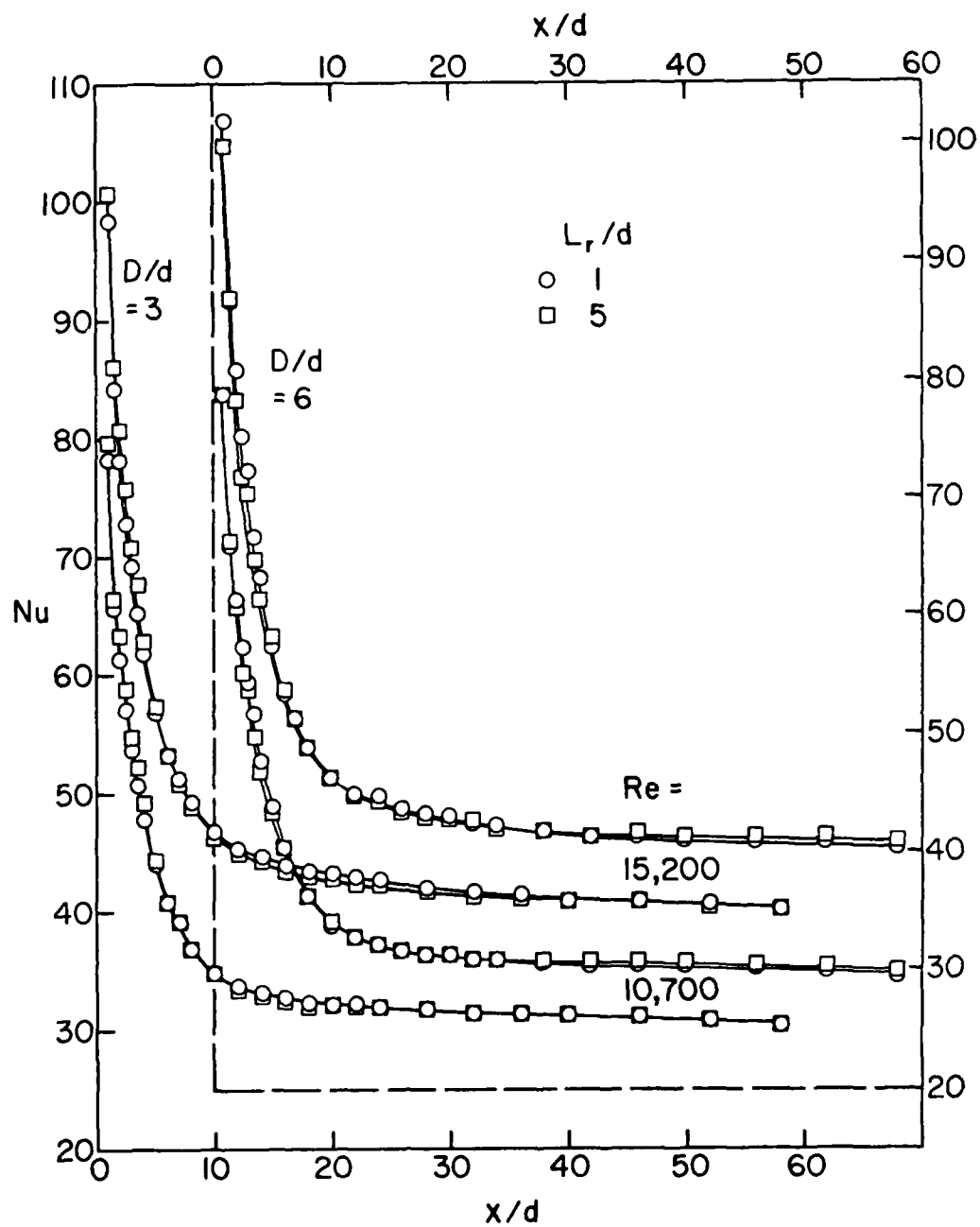


Fig. 6

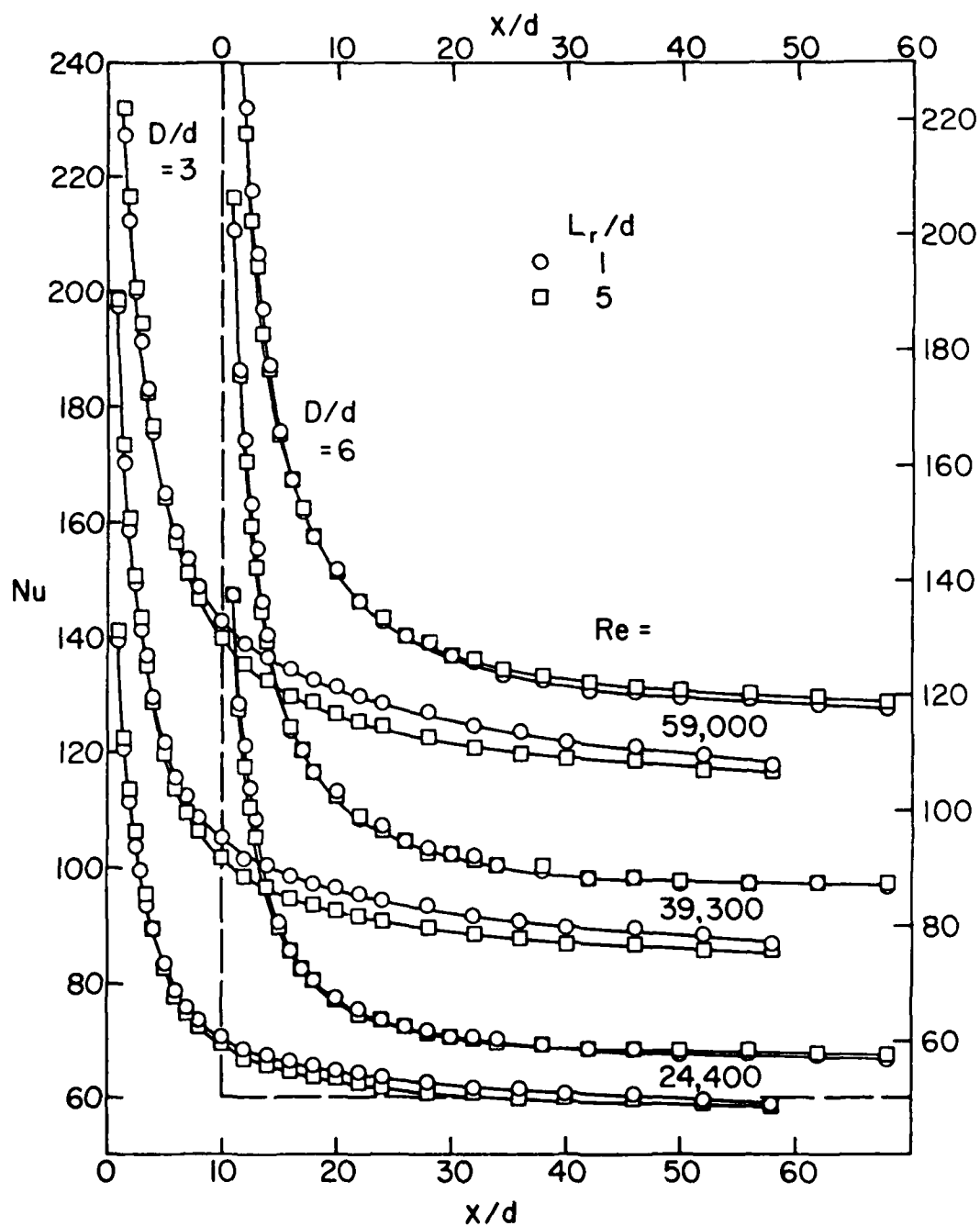


Fig. 7

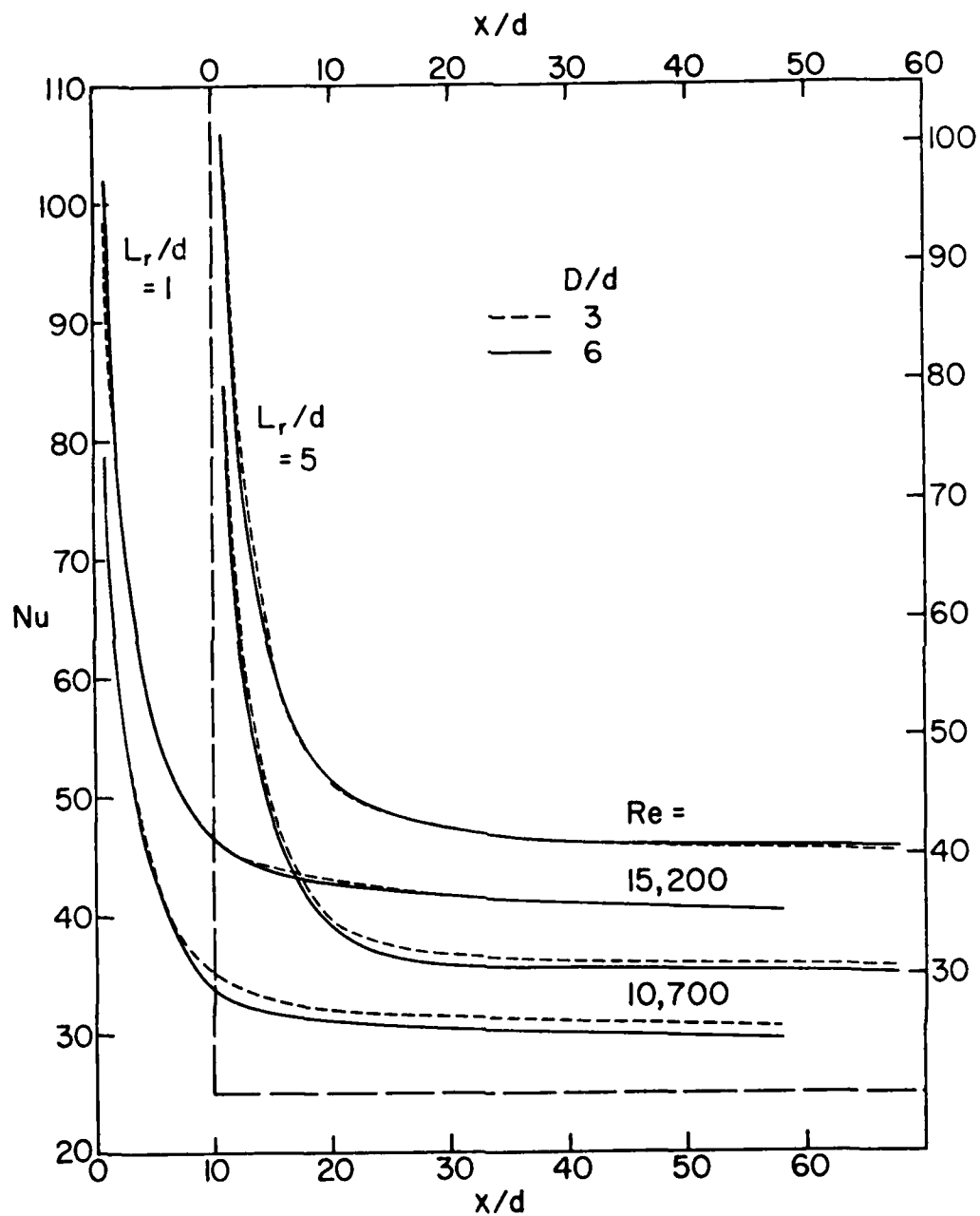


Fig. 8

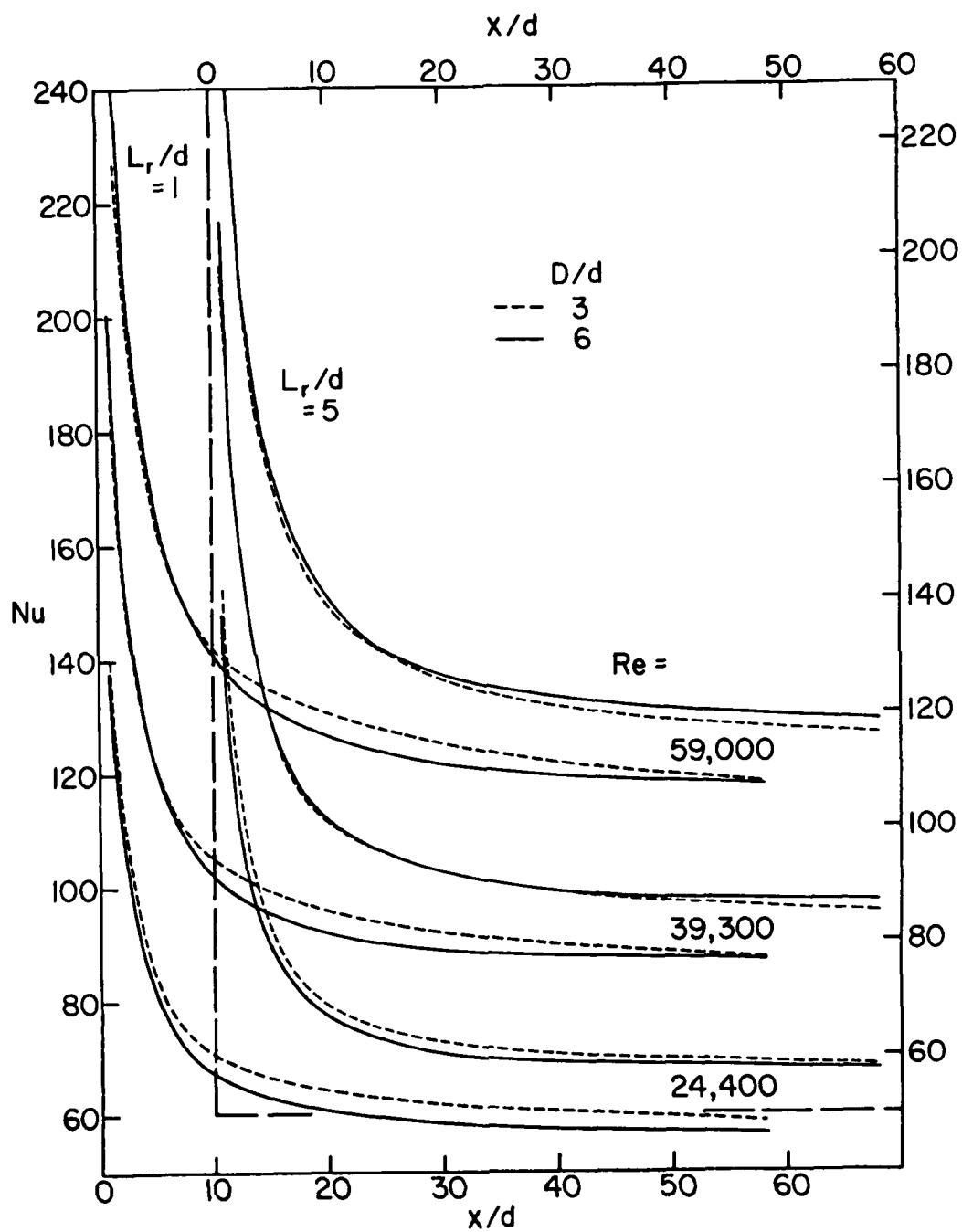


Fig. 9

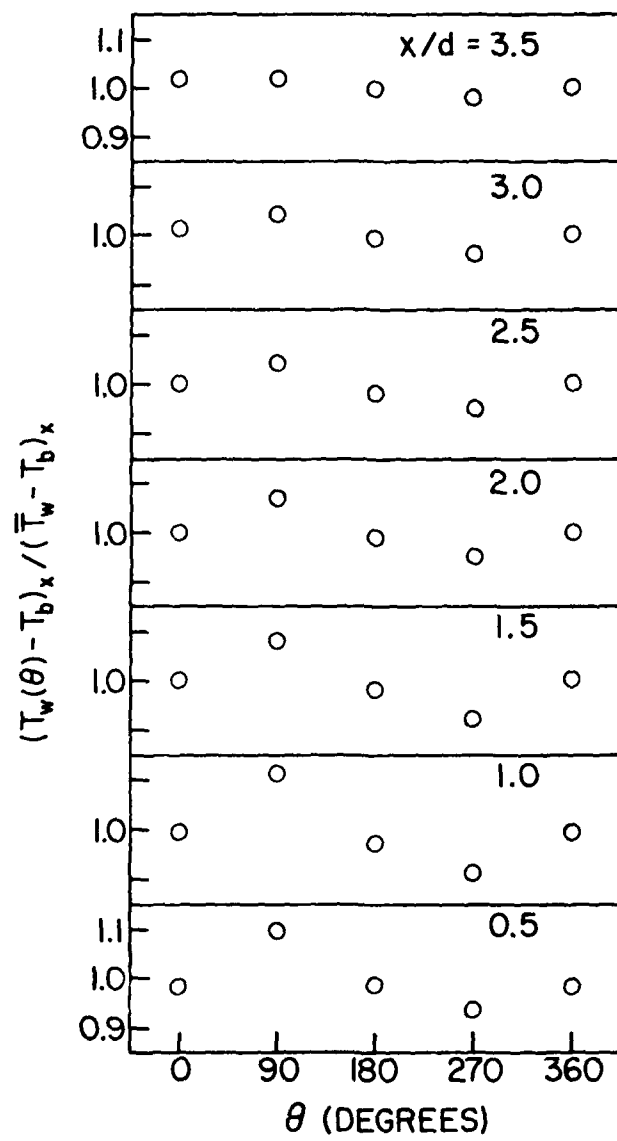


Fig. 10

Chapter 3

EFFECT OF A MISSING CYLINDER ON HEAT TRANSFER AND FLUID FLOW
IN AN ARRAY OF CYLINDERS IN CROSSFLOW

INTRODUCTION

There is a substantial literature on heat exchange devices which encompass arrays of cylinders in crossflow {1 - 3}. Without exception, the available information pertains to regular arrays in which all elements of the array are present. The present investigation deals with departures from regularity, with specific consideration being given to the effect of a missing cylinder on the heat transfer and fluid flow characteristics of adjacent cylinders. The investigation has two parts. In one part, quantitative heat transfer measurements were made for cylinders that are situated adjacent to the site of the missing cylinder. In the other part, flow visualization was performed to explore the manner in which the fluid flow pattern in the array is affected by the missing cylinder. Experiments were conducted for both staggered and in-line arrangements.

THE EXPERIMENTS

The host flow passage for the array of cylinders was a flat rectangular duct, 8.26 x 1.91 cm (width x height) in cross section, and 173 cm long. The overall length of the duct encompassed a hydrodynamic development section, the test section, and a downstream hydrodynamic redevelopment section.

The cylinders comprising the array were oriented perpendicular to the principal walls of the test section (i.e., the upper and lower walls) and were seated in holes in the lower wall. Interchangeable lower walls were fabricated with suitable hole arrangements to accommodate the in-line and staggered arrays. The staggered array was laid out in an equilateral-triangular pattern, with $S_T/D = 3$ and $S_L/D = (\sqrt{3}/2)(S_T/D)$.

where S_T and S_L are the transverse and longitudinal pitches, and $D = 0.556$ cm is the cylinder diameter. The in-line array was, in effect, a realignment of the staggered array with the values of S_T/D and S_L/D being maintained. In both cases, eighteen rows of cylinders were employed. The heat transfer measurements were made in the twelfth row, where fully developed conditions prevailed.

The cylinders used in the experiments were intended to model pin fins, and a small clearance gap ($1/8$ of the channel height) was left between the tips of the cylinders and the upper wall of the test section. Experiments reported in {4} and {5}, where the aforementioned staggered and in-line arrays were respectively employed in a fully populated state (without missing cylinders), yielded fully developed heat transfer coefficients that agreed very well with literature values for tube banks. On this basis, the present results for the effects of missing cylinders should also be relevant to tube banks. Air was the working fluid in all of the experiments.

Instead of direct heat transfer measurements, per-cylinder heat transfer coefficients were deduced by applying the heat/mass transfer analogy to mass transfer measurements performed via the naphthalene sublimation technique. The procedures for applying this technique for cylindrical pin fins are documented in {4}, as is the data reduction process which converts mass transfer measurements to mass transfer coefficients and, by the analogy, to heat transfer coefficients.

The flow visualization was performed by means of the oil-lampblack technique. To facilitate the use of this technique, the lower wall of the test section was covered with white, plastic-coated contact paper, and holes were cut in the paper to accommodate the array of cylinders. Before insertion of the cylinders, the contact paper was brushed with a mixture of lampblack powder and oil of suitable consistency. Once the cylinders were inserted, the test section was sealed and the airflow activated. Under the action of the shear stresses exerted by the airflow, the oil-lampblack mixture was caused to move, thereby revealing the pattern of fluid flow adjacent to the lower wall of the test section.

RESULTS AND DISCUSSION

Flow visualization. The flow visualization photographs presented in Figs. 1(a) and (b) and in 2(a) and (b) convey a record of the pattern of fluid flow adjacent to the lower wall of the test section. Each figure is a top view looking downward on the array, with the white circles corresponding to the locations of the cylinders and with the fluid flowing in the direction from the bottom to the top of the photograph. Figures 1(a) and (b) pertain to the staggered array. The first of these shows all of the cylinders in place, while in the second, one of the cylinders of the array is missing. Similarly, Figs. 2(a) and (b) pertain to the in-line array, respectively for all cylinders in place and for one cylinder missing.

In interpreting these photos, it should be noted that prior to the onset of the airflow, the entire field, except for the white circles, is a uniform, glossy black. The white streaks in evidence in the photos correspond to the path lines of the fluid flow, while zones of concentrated black color depict regions where the shear exerted by the fluid was too weak to move the oil-lampblack mixture. These black zones may be regarded as indicating low velocity regions.

In this regard, a special note of caution should be sounded about the somewhat irregular black annuli which surround the various holes. The respective annuli result, in large part, from an accumulation of the black mixture which was swept up against the cylinder when the airflow was initiated and was held there by the forces exerted by the flow. When the airflow was turned off, the mixture drained from the cylinder (due to gravity) and formed the black annulus.

Examination of Fig. 1(a) reveals a remarkable regularity, both among the successive rows and across the span of the array in any given row (irregularities in the black annuli are extraneous, as just discussed). The row-by-row repetition of the flow pattern typifies the periodic fully developed regime. Regions of low velocity (i.e., black regions) exist both upstream and downstream of each cylinder in the array. The low velocity region upstream of the cylinder is due to the collision of

two flows. One of these is the mainflow approaching the cylinder. The other is a backflow which is induced by a gradient of pressure along the height of the cylinder. This pressure gradient drives fluid downward along the cylinder, causing it to splash against the lower wall of the test section. Part of the splashed flow moves forward into the path of the mainflow which passes adjacent to the wall, and the opposing flows create a low-velocity region.

The low-velocity region downstream of the cylinder is a buffer zone (i.e., an island of calm) between the recirculating flow situated immediately downstream of the cylinder and the mainflow which threads its way through the alley between diagonally positioned cylinders. The recirculating flow is readily identified by examination of the crown-like structure perched atop each cylinder (i.e., just downstream of the cylinder). The side-to-side symmetry of the crown is another indication of the span-wise periodicity of the flow field.

Figure 1(b), when compared with Fig. 1(a), provides an indication of the alteration of the flow which occurs when a cylinder is missing. The disturbance of the flow is seen to be quite localized. Fluid tends to pass longitudinally through the space formerly occupied by the now-missing cylinder, and it is evident that the flow adjacent to the two cylinders at the downstream end of the straight run is definitely affected, as witnessed by the outward canting of the crowns of these cylinders. Otherwise, the flow field does not seem to be much different from that pictured in Fig. 1(a).

For the fully populated in-line array, (Fig. 2(a), the expected tendency of the mainflow to course through the clear channels and to ignore the longitudinal inter-cylinder spaces is vividly displayed. The mainflow acknowledges the presence of the successive rows of cylinders by adopting a slightly undulating path, which pinches in when abreast of the cylinders and spreads out slightly when abreast of the inter-cylinder space. The fore portion of the intercylinder space is dominated by a recirculation zone while the aft portion (the black region) is a low-velocity zone.

The removal of a cylinder, Fig. 2(b), enables the mainflow to make a somewhat

deeper incursion into the now-elongated intercylinder space. It is noteworthy, however, that the crowns of the two cylinders which stand at the right-hand and left-hand sides of the vacated space are not skewed, suggesting a minimal effect on these cylinders. The crown of the cylinder just upstream of the space is slightly truncated compared to the normal pattern, as is the low-velocity region at the downstream end of the space. From the photographs alone, it is difficult to assess the importance of these seemingly minor changes.

Heat transfer results. The heat transfer results are presented in Figs. 3 and 4, respectively for the staggered and in-line arrays. Each figure displays the portion of the array which encompasses the missing cylinder, with the flow direction being from left to right as shown. As noted earlier, the heat transfer coefficients were measured in the twelfth row and correspond to the fully developed regime.

In each figure, each of the cylinders situated in the neighborhood of the site of the missing cylinder is marked with two numbers, one above and one below. Each number represents the ratio of two heat transfer coefficients, with both coefficients corresponding to a given Reynolds number. The numerator of the ratio is the heat transfer coefficient for the case in which there is a cylinder missing from the array, while the denominator is the heat transfer coefficient when all cylinders are present. Thus, the departures of the listed ratios from unity provide an immediate measure of the effect of the missing cylinder.

The results are parameterized by the Reynolds number, for which two distinct definitions have been employed. One of the Reynolds numbers is that for the duct without the cylinders in place. The other Reynolds number is based on the velocity through the minimum flow area of the array and on the cylinder diameter as the characteristic dimension. The two duct Reynolds numbers considered were 5000 and 35,000, with corresponding array Reynolds numbers of 1270 and 8900. In the figures, the numbers listed above the respective cylinders correspond to the higher of the two Reynolds numbers, while the numbers listed below are for the lower Reynolds number.

Turning first to the staggered array, Fig. 3, it is seen that the missing cylinder tends to reduce the heat transfer coefficients at the neighboring cylinders, but for the most part, the reductions are very small. For cylinders located either to the side or forward of the vacated site, the reductions are in the 0-3 percent range. Only in the row immediately downstream of the vacated site is there a noteworthy effect--a ten percent reduction at the higher Reynolds number. This reduction in the value of the transfer coefficient is the result of a lower impingement velocity and of a possible reduction of the turbulence level. That this row should be the most affected by the missing cylinder is in accord with comments made during the discussion of the flow visualization photographs.

Lesser reductions occur both to the side of the vacant site and at two rows downstream. These reductions are smaller because at these locations, either a decrease in velocity or lower turbulence may play a role, but both do not act simultaneously. The heat transfer coefficients at the lower Reynolds number appear to be less affected by the missing cylinder than are those at the higher Reynolds number.

Figure 4 shows that the heat transfer coefficients for the in-line array are quite insensitive to the missing cylinder. This finding is not surprising in light of the minimal modification of the flow field which occurs when a cylinder is removed from the array (Figs. 2(a) and (b)).

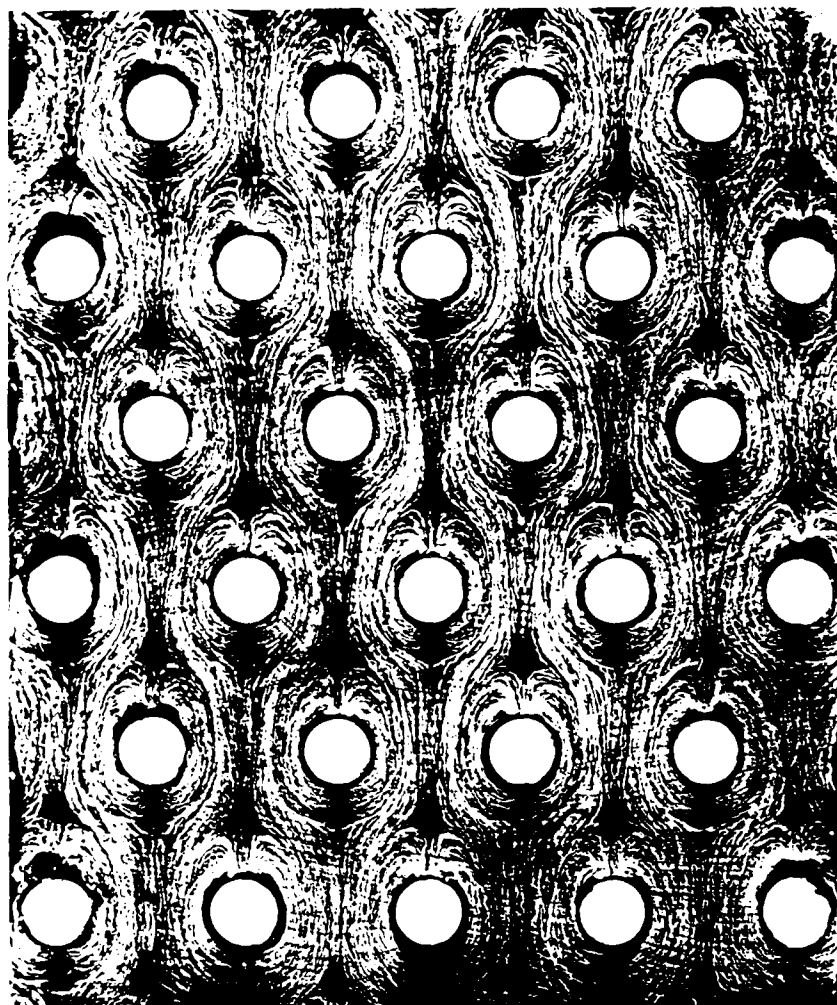
In general, the irregularity caused by a missing cylinder does not result in significant changes in the heat transfer coefficients at the neighboring cylinders of the array.

REFERENCES

1. Kays, W. M. and London, A. L., Compact Heat Exchangers, Second ed., McGraw-Hill, New York, 1964.
2. Fraas, A. P. and Ozisik, M. N., Heat Exchanger Design, Wiley, New York, 1965.
3. Zhukauskus, A. A., "Heat Transfer from Tubes in Crossflow," in Advances in Heat Transfer, Vol. 8, Academic Press, New York, 1972, pp. 93-106.
4. Sparrow, E. M. and Ramsey, J. W., "Heat Transfer and Pressure Drop for a Staggered Wall-Attached Array of Cylinders with Tip Clearance," International Journal of Heat and Mass Transfer, Vol. 21, 1978, pp. 1369-1378.
5. Sparrow, E. M., Ramsey, J. W., and Altemani, C.A.C., "Experiments on In-Line Pin Fin Arrays and Performance Comparisons with Staggered Arrays," Journal of Heat Transfer, Vol. 102, 1980, pp. 44-50.

FIGURE CAPTIONS

- Fig. 1(a) Fluid flow pattern for a fully populated staggered array
- Fig. 1(b) Fluid flow pattern for a staggered array in which there is a cylinder missing from the array
- Fig. 2(a) Fluid flow pattern for a fully populated in-line array
- Fig. 2(b) Fluid flow pattern for an in-line array in which there is a cylinder missing from the array
- Fig. 3 Effect of a missing cylinder on the heat transfer coefficients at neighboring cylinders in a staggered array
- Fig. 4 Effect of a missing cylinder on the heat transfer coefficients at neighboring cylinders in an in-line array



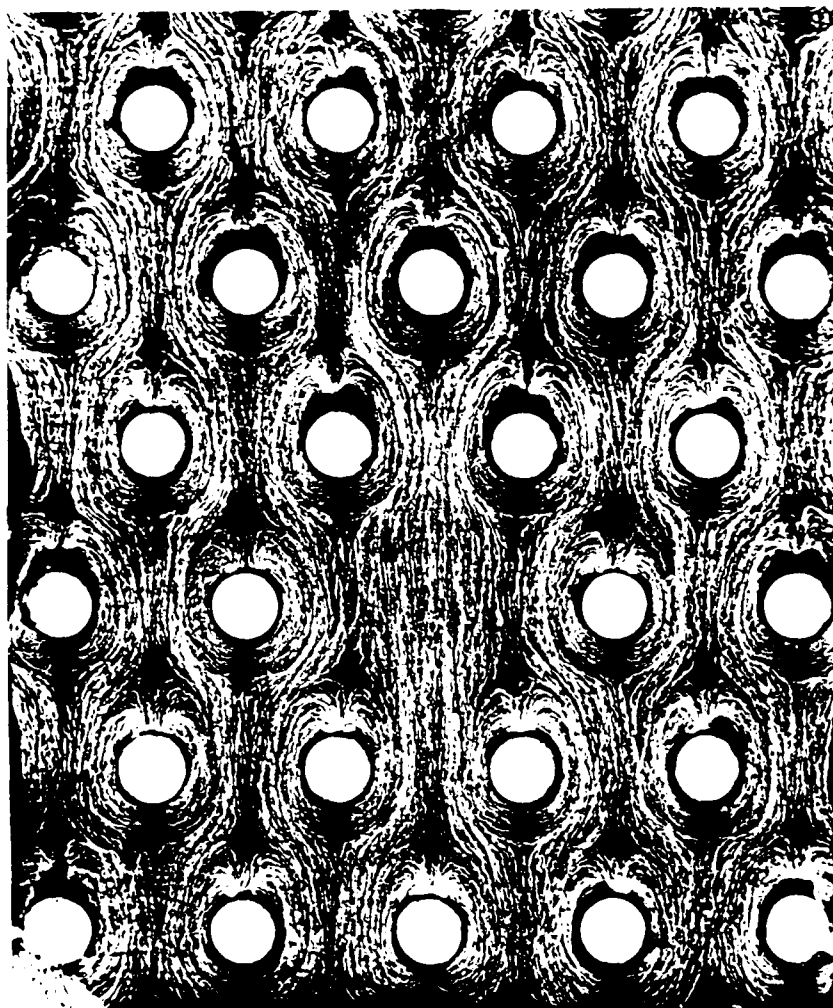


Fig. 1(b)

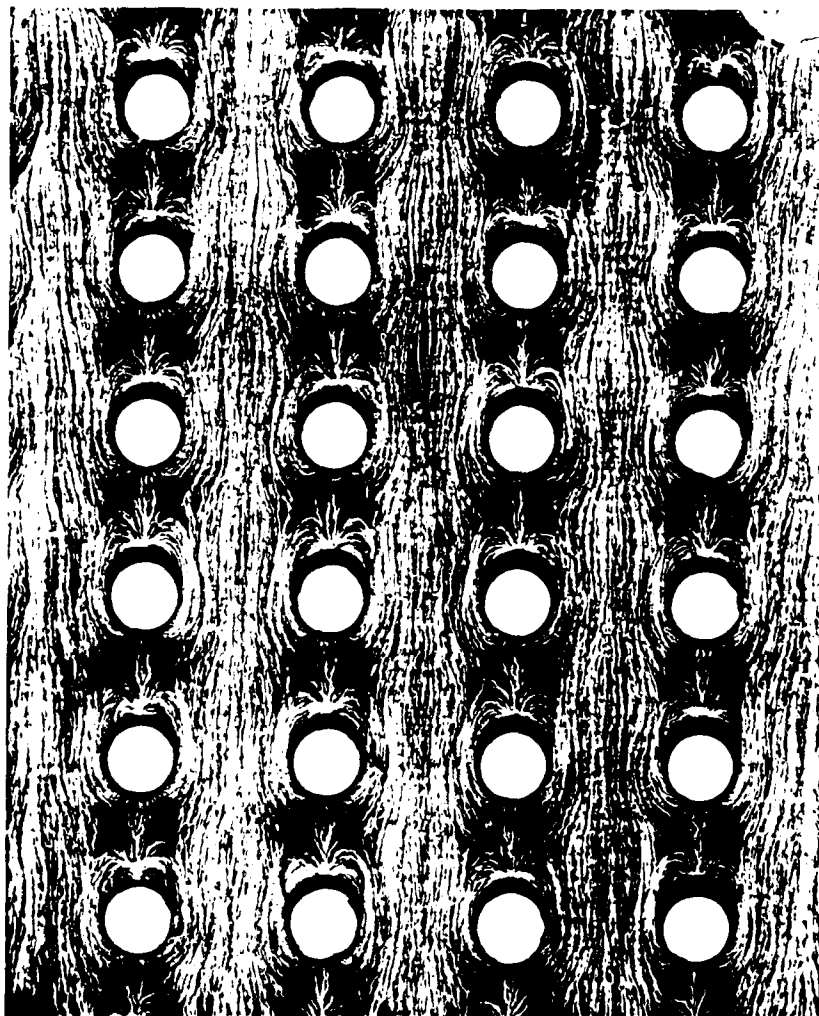


Fig. 2(n)

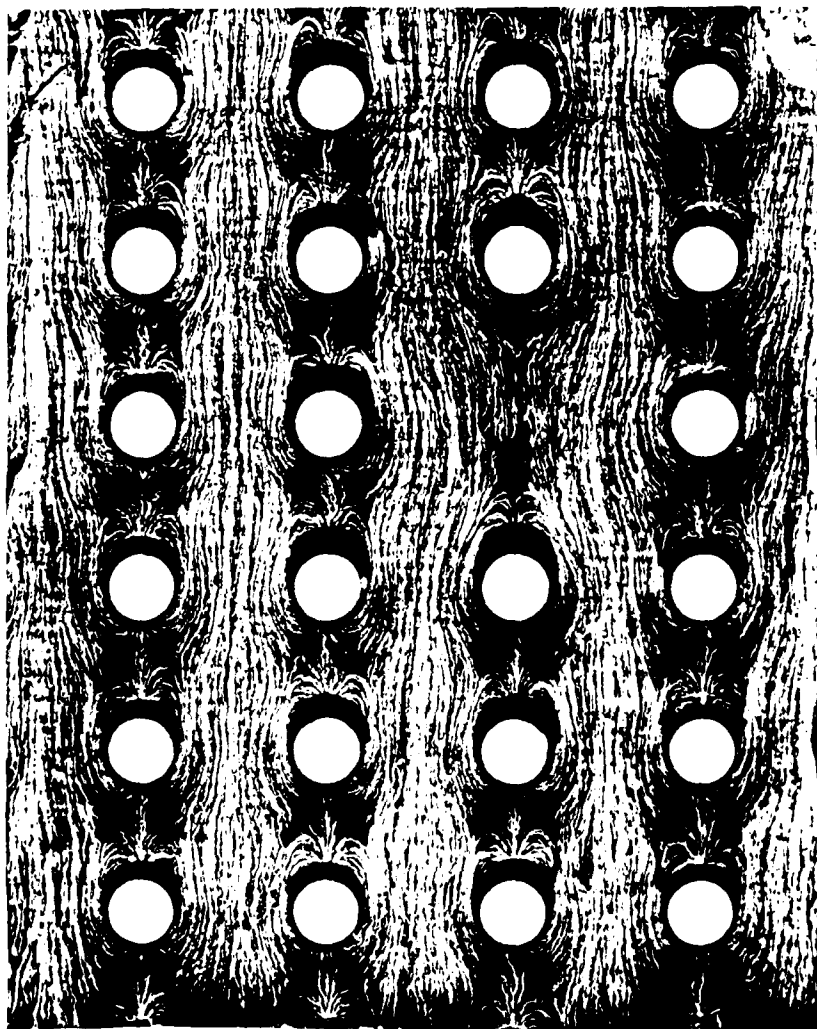


Fig. 2(b)

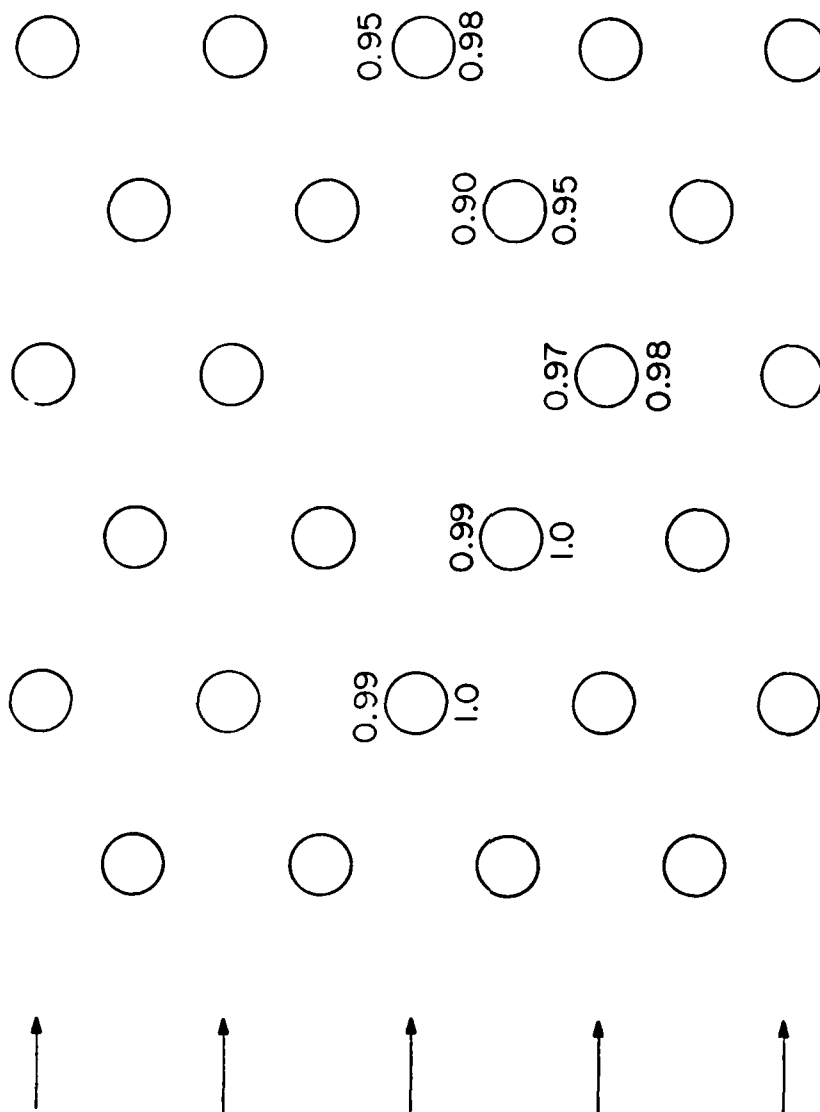


Fig. 3

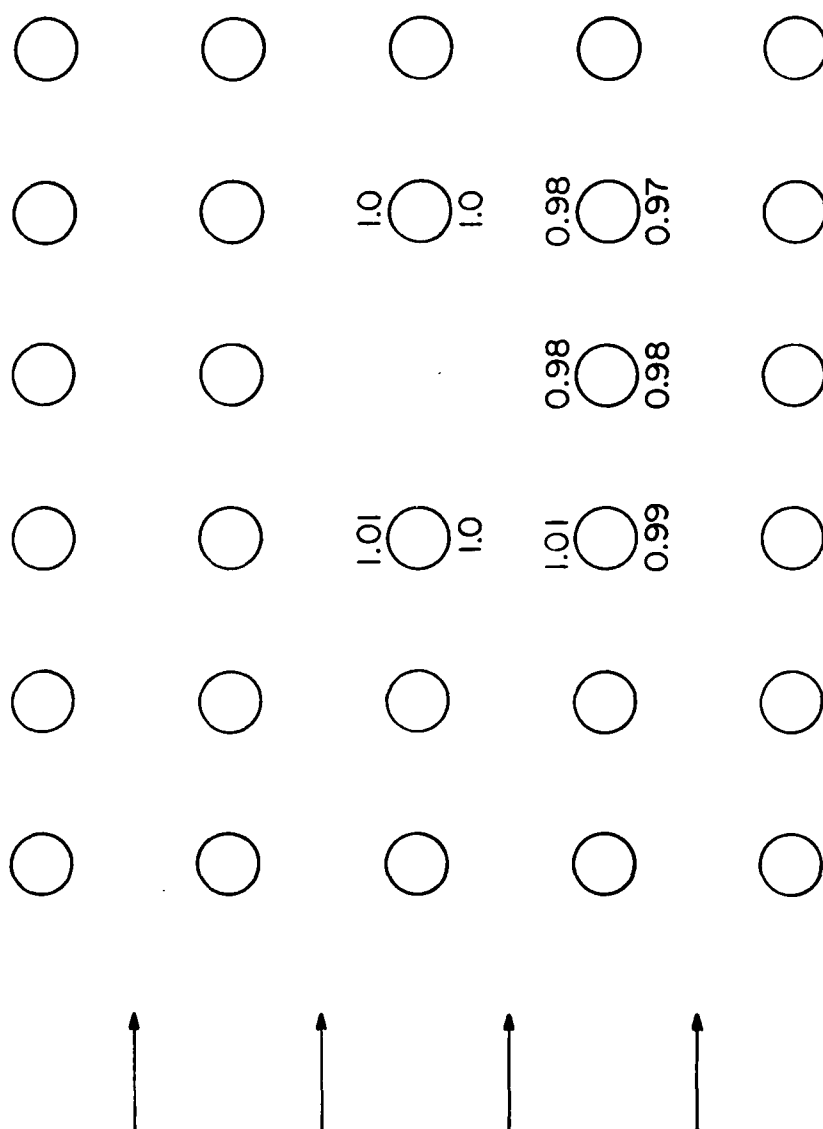


Fig. 4

Chapter 4

PREDICTION OF THE TURBULENT FLOW
IN A CYLINDRICAL PLENUM

NOMENCLATURE

c_1, c_2, c_μ	constants in the turbulence model
d	diameter of the inlet and exit pipes
D	diameter of the plenum
G	generation rate of turbulence energy, equation (7)
K	pressure-loss coefficient, $\Delta p / (\rho V^2 / 2)$
k	turbulence kinetic energy
L	length of the plenum
p	pressure
Δp	pressure drop across the plenum
Re	Reynolds number, $\rho V d / \mu$
u_i	velocity component in the i direction
V	mean velocity in the inlet pipe
x_i	coordinate in the i direction
ϵ	dissipation rate of turbulence energy
μ	laminar viscosity
μ_t	turbulent viscosity
ρ	density
$\sigma_k, \sigma_\epsilon$	constants in the turbulence model
τ_{ij}	turbulent stress
ψ^+	dimensionless stream function

INTRODUCTION

Piping systems often include various fittings, joints, and plenums. These contribute to the pressure drop and flow distortion. The purpose of the present investigation is to predict the turbulent flow field and the associated pressure drop in a cylindrical plenum. The geometry of the plenum and the inlet and exit pipes is shown in Fig. 1. These pipes are coaxial with the plenum and have a diameter of d . The diameter and the length of the plenum are denoted by D and L respectively. This configuration is chosen for numerical computation because experimental measurements for the same configuration are available from {1}.

The recirculating flow in the plenum was computed on the basis of the $k-\epsilon$ model of turbulence, in which differential equations for the kinetic energy of turbulence and for its dissipation rate were solved.

MATHEMATICAL FORMULATION

Governing equations. The two-dimensional flow field in the chosen configuration is governed by the continuity equation and the momentum equations. The density is regarded as constant. The governing equations can be compactly stated in the Cartesian-tensor form as follows.

$$\text{Continuity: } \partial u_i / \partial x_i = 0 \quad (1)$$

$$\text{Momentum: } \rho u_i (\partial u_j / \partial x_i) = \partial \tau_{ij} / \partial x_i - \partial p / \partial x_j \quad (2)$$

Here u_i stands for the time-averaged velocity component in the i direction and the τ 's are the turbulent stresses; the corresponding laminar stresses are assumed to be negligible everywhere except near the walls. The turbulent stresses are evaluated by means of a turbulence model.

Turbulence model. The turbulent stresses are first expressed in terms of a turbulent viscosity μ_t and the velocity gradients. The expression in the Cartesian-tensor form is

$$\tau_{ij} = \mu_t (\partial u_i / \partial x_j + \partial u_j / \partial x_i) - (2/3) \rho k \delta_{ij} \quad (3)$$

where δ_{ij} is the Kronecker delta and k is the kinetic energy of turbulence.

The turbulent viscosity μ_t is further expressed in terms of k and the dissipation rate of k , which is denoted by ϵ . The expression for μ_t is

$$\mu_t = c_\mu \rho k^2 / \epsilon \quad (4)$$

where c_μ is a constant.

The two-equation turbulence model of {2} provides two differential equations for the turbulence parameters k and ϵ . They are

$$\rho u_i \partial k / \partial x_i = \partial / \partial x_i ((\mu_t / \sigma_k) \partial k / \partial x_i) + G - \rho \epsilon \quad (5)$$

$$\rho u_i \partial \epsilon / \partial x_i = \partial / \partial x_i ((\mu_t / \sigma_\epsilon) \partial \epsilon / \partial x_i) + (c_1 G - c_2 \rho \epsilon) (\epsilon / k) \quad (6)$$

The quantity G is the rate of generation of k by the action of velocity gradients.

The expression for G is given by

$$G = \mu_t (\partial u_i / \partial x_j + \partial u_j / \partial x_i) (\partial u_i / \partial x_j) \quad (7)$$

The turbulence model involves five empirical constants. The values used in the present work are those recommended in {2}; they are:

$$c_\mu = 0.09, \quad c_1 = 1.44, \quad c_2 = 1.92, \quad \sigma_k = 1.0, \quad \sigma_\epsilon = 1.3$$

It should be noted here that these constants have successfully been used for a wide variety of physical situations to obtain satisfactory agreement with experimental data.

Region near the walls. Since the laminar stresses become important in the low-Reynolds-number region near solid walls, a special treatment is needed there. In the present work, the wall-function technique outlined in {2} was used. It amounts to the assumption that the universal logarithmic velocity profile exists in the near-wall region and that the length scale there is proportional to the distance from the wall.

Inlet conditions. The values of the turbulence parameters k and ϵ in the

inlet stream were taken to be those appropriate to the turbulent fully developed pipe flow. However, the results were not sensitive to the inlet values of k and ϵ . This is because so much more turbulence is generated in the plenum that the behavior of the flow field depends little on the amount of turbulence energy convected by the inlet stream.

Numerical solution. The foregoing differential equations were solved in the domain of interest by the finite difference method described in {3}. In particular, the SIMPLER procedure was used to solve the coupled momentum and continuity equations. A 22×22 grid was used. Some exploratory computations indicated that this grid gave results of sufficient accuracy.

RESULTS

Pressure drop. The total pressure drop Δp between the inlet and the exit of the plenum can be expressed in terms of a loss coefficient K defined as $\Delta p / (\rho V^2 / 2)$, where V is the average inlet velocity. The predicted values of K are compared in Fig. 2 with the experimental data from {1}, for two values of L/d and two values of D/d . It should be mentioned that, whereas the computed values of K are based on the pressure drop in only the plenum region, the measured values of K take some account of the additional pressure drop in the inlet and exit pipes. However, these additional pressure drops are expected to be small; therefore, the comparison is meaningful. As seen from Fig. 2, the computed results agree reasonably well with the experimental data.

Streamline patterns. The velocity field in the plenum is presented in Figs. 3 and 4 in the form of streamlines. There is a basic throughflow from inlet to exit, and a recirculating flow can be seen to have formed in the plenum region. The strength of the recirculating flow can be judged from the values of ψ^+ , which is a dimensionless stream function defined such that the throughflow has a ψ^+ value of unity. For the two configurations shown in Fig. 3, the

recirculating flow rate is about 50% of the rate of the throughflow. In Fig. 4, the plenum has a much bigger diameter than do the inlet and exit pipes. This tends to produce greater recirculating flow. For $L/d = 5$, the recirculating flow is twice as large as the throughflow. However, for $L/d = 1$, the plenum is so narrow that it restricts the recirculating flow to only about 50% of the throughflow.

CONCLUDING REMARKS

The recirculating flow in a cylindrical plenum has been computed by a numerical method. The calculation employs the well-known $k-\epsilon$ model with the standard set of empirical constants. The predicted pressure drop agrees well with the experimental data. The streamline patterns are presented; they indicate the strength of the recirculating flow.

REFERENCES

1. Lau, S. C., Sparrow, E. M., and Ramsey, J. W., "Effect of Plenum Length and Diameter on Turbulent Heat Transfer in a Downstream Tube and on Plenum-Related Pressure Losses," *Journal of Heat Transfer*, vol. 103, pp. 415-422, 1981.
2. Launder, B. E. and Spalding, D. B., "The Numerical Computation of Turbulent Flows," *Comp. Methods Appl. Mech. Eng.*, vol. 3, pp. 269-289, 1974.
3. Patankar, S. V., Numerical Heat Transfer and Fluid Flow, McGraw-Hill-Hemisphere, 1980.

FIGURE CAPTIONS

- Fig. 1 The cylindrical plenum
- Fig. 2 Comparison of the predicted pressure-loss coefficient
 with experimental data
- Fig. 3 Streamline patterns for $D/d = 3$ and $Re = 20,000$
- Fig. 4 Streamline patterns for $D/d = 6$ and $Re = 20,000$

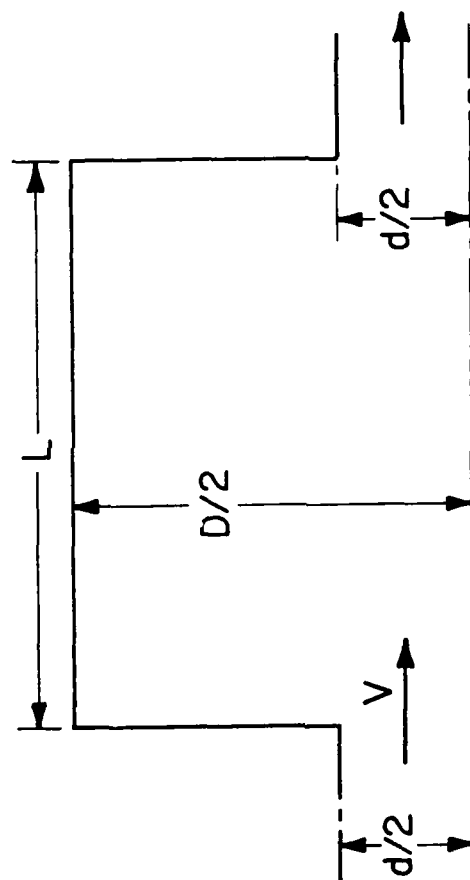


Fig. 1

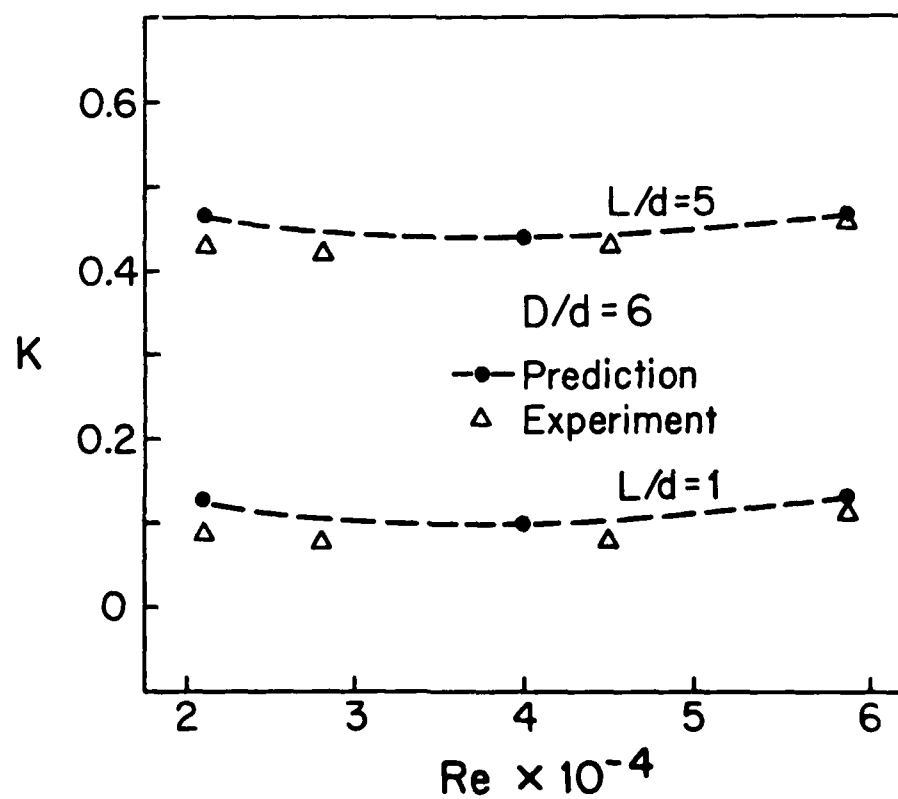
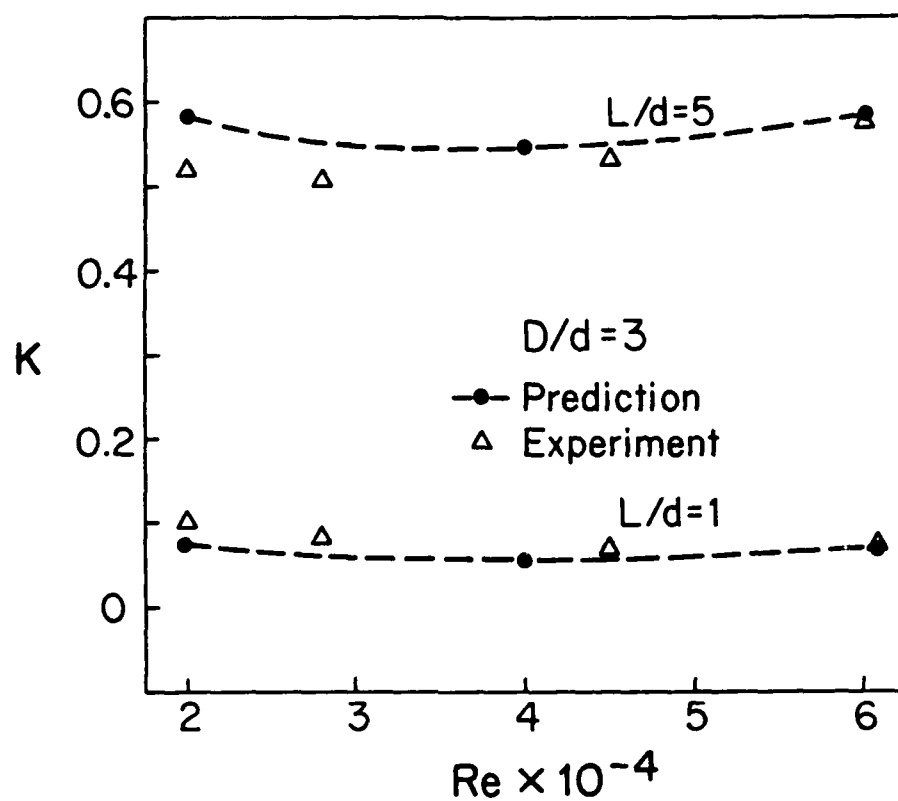


Fig. 2

AD-A110 396

MINNESOTA UNIV MINNEAPOLIS DEPT OF MECHANICAL ENGIN--ETC F/G 20/13
STUDIES OF HEAT TRANSFER IN COMPLEX INTERNAL FLOWS.(U)
JAN 82 E M SPARROW, S V PATANKAR

N00014-79-C-0621

NL

UNCLASSIFIED

2 OF 2

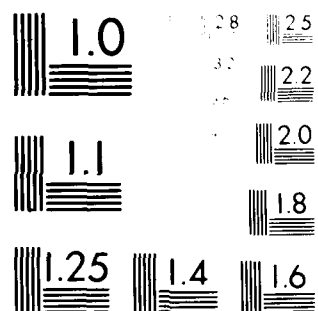
AD-A
CAGR

END

DATE
FILMED

02 82

DTIC



MICROCOPY RESOLUTION TEST CHART

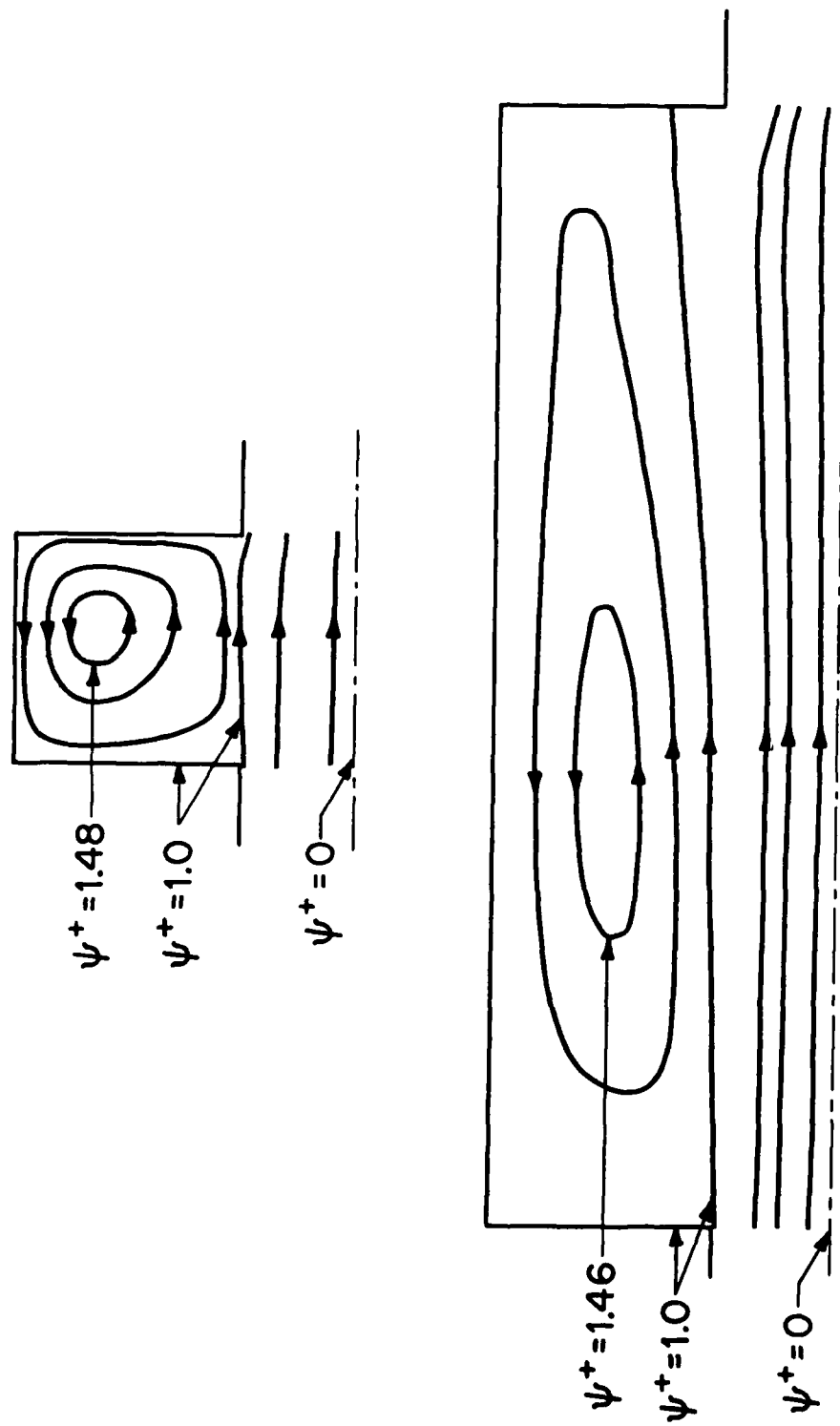


Fig. 3

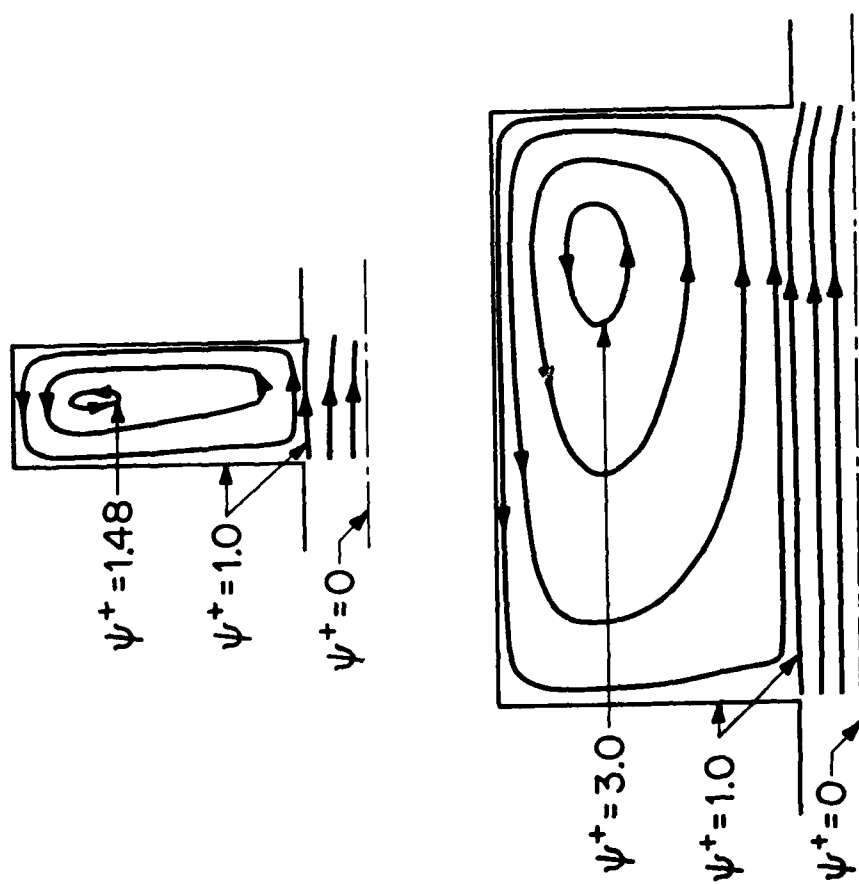


Fig. 4

Chapter 5

PREDICTION OF FLOW MALDISTRIBUTION IN A
TUBE BUNDLE PLACED IN A FLOW WITH SUDDEN EXPANSION

NOMENCLATURE

d	tube diameter, Fig. 1
f	friction factor, equation (4)
h	inlet dimension, Fig. 1
H	half width of the channel, Fig. 1
L_1	length of the free region, Fig. 1
L_2	length of the tube bundle, Fig. 1
p	pressure
P	pitch of the tube arrangement, Fig. 1
R_j	resistance in the j direction
u	velocity in the x direction
u_i	velocity in the i direction
U	inlet velocity, Fig. 1
V	magnitude of the local velocity vector
x_i	coordinate in the i direction
x, y	Cartesian coordinates
μ	viscosity
ρ	density

INTRODUCTION

Heat exchangers often consist of a tube bundle placed in a cross stream. The design of the heat exchanger or an estimate of its performance is usually based on the assumption that the tube bundle experiences a uniform flow over it. However, the actual flow distribution depends upon the geometrical details of the inlet configuration. For example, in the situation outlined in Fig. 1, the tube bundle is situated in a plane channel in which the inlet flow undergoes a sudden expansion before entering the bundle. Thus, it is possible that most of the flow washes the center of the bundle, while the edges of the bundle receive only a weak flow. Such maldistribution of flow adversely affects the performance of the heat exchanger, since the tubes in the edge regions become virtually ineffective. Overheating of tubes can also result in the local regions of insufficient cross flow.

The present investigation is intended to demonstrate the use of a numerical technique in predicting the flow maldistribution resulting from the sudden enlargement of the inlet flow.

The flow in the open region of length L_1 in Fig. 1 is calculated as a regular turbulent flow described by the $k-\epsilon$ model. The flow in the tube bundle region of length L_2 is treated by the distributed-resistance concept introduced in [1].

FORMULATION

The mathematical framework for the turbulent flow in the open region of sudden expansion is identical to the formulation used for the plenum flow in Chapter 4 of this report. Therefore, that description will not be repeated here. Now attention will be turned to the distributed-resistance model for the tube-bundle region.

For a medium of uniform porosity, the flow is governed by the continuity and momentum equations, which can be written as follows:

$$\text{Continuity: } \partial u_i / \partial x_i = 0 \quad (1)$$

$$\text{Momentum: } \rho u_i \partial u_j / \partial x_i = \partial p / \partial x_j + R_j \quad (2)$$

where R_j is the distributed-resistance force per unit volume.

For the staggered tube bank shown in Fig. 1, the distributed resistance can be obtained from the empirical correlations given by McAdams {2}. The formula used in the present work is

$$R_j = -2\rho(f/P)Vu_j \quad (3)$$

Here P is the pitch of the tube arrangement, V is the magnitude of the resultant velocity vector, and f is the friction factor given by

$$f = \{0.23 + 0.11/((3P/d)^{1/2} - 1)^{1.08}\}(\rho Vd/\mu)^{-0.15} \quad (4)$$

The negative sign in equation (3) indicates the resistance force opposes the momentum u_j rather than assists it.

The resulting set of nonlinear coupled partial differential equations was solved by the numerical method described in {3}.

RESULTS

The numerical solutions were obtained to illustrate the kind of flow maldistribution that can be predicted with the proposed mathematical model. With reference to Fig. 1, the expansion ratio h/H was held at 0.5. The inlet flow was characterized by a Reynolds number $\rho U h / \mu$, which was set equal to 2.5×10^6 . The tube bundle was composed of a triangular array of tubes with $P/d = 1.6$. The number of tubes was determined by $H/P = 50$. The lengths L_1 and L_2 were varied to study their effect on the flow distribution.

The nature of the flow in the tube bundle can be observed by examining the profiles of the x -direction velocity u at three chosen locations 1, 2, and 3 as shown in Fig. 1.

The effect of the tube-bundle length. The first set of computations were

performed for a fixed length L_1 of the free region. L_1 was set equal to H . The length L_2 of the tube bundle was varied. The resulting profiles of u at the three stations are shown in Fig. 2.

A long tube bundle represents a large flow resistance, which has the effect of ensuring an almost uniform flow through the bundle. A short bundle, on the other hand, is more susceptible to the details of the inlet configuration. This behavior is clearly seen in Fig. 2. When L_2/H is equal to 1 or 2, the velocity distribution is almost uniform. For small values of L_2/H , large nonuniformities are present in the velocity profiles. The part of the bundle directly in front of the restricted inlet receives high velocity fluid, while the region near the channel wall is washed by much slower flow. Of course, the flow nonuniformities are most severe at the inlet of the bundle (i.e., around station 1). As the flow moves through the bundle, the velocity distribution becomes more uniform.

The effect of the location of the tube bundle. Since in the situation considered the flow nonuniformity is caused by the sudden expansion of the inlet flow, the proximity of the tube bundle to the inlet is also an important factor. A set of computations were performed to investigate this effect. Here, the bundle length L_2 was set equal to H , while the free length L_1 was varied. The case of $L_1/H = 1$ and $L_2/H = 1$ has been reported in Fig. 2, for which the flow nonuniformity was rather small. Greater nonuniformity is produced by smaller values of L_1/H , i.e., by locating the tube bundle closer to the inlet.

Figure 3 shows the velocity profiles at the three stations for different values of L_1/H . The flow nonuniformity is very striking especially at $L_1/H = 0.1$. It is as if the inlet flow moves straight ahead in the central region without taking advantage of the expanded flow area. Once again, the flow nonuniformity gradually becomes less severe as the fluid moves from station 1 to station 3.

CONCLUDING REMARKS

A mathematical model has been formulated to predict the flow nonuniformity in a tube bundle placed in a flow with sudden expansion. The model consists of a regular turbulent flow computation in the upstream region and a distributed-resistance calculation in the bundle region. Illustrative results show the flow maldistribution present in tube bundles of various lengths. Also, the effect of locating the bundle at different distances from the inlet is investigated. The results of such computations are expected to be useful in predicting heat exchanger performance and bundle vibrations.

REFERENCES

1. Patankar, S. V. and Spalding, D. B., "A Calculation Procedure for the Transient and Steady-State Behavior of Shell-and-Tube Heat Exchangers," in *Heat Exchangers: Design and Theory Sourcebook*, Scripta Book Company, Washington, D.C., 1974.
2. McAdams, W. H., Heat Transmission, 3rd Ed., McGraw-Hill, New York, 1954.
3. Patankar, S. V., Numerical Heat Transfer and Fluid Flow, McGraw-Hill-Hemisphere, 1980.

FIGURE CAPTIONS

- Fig. 1 Tube bundle in a sudden-expansion flow
- Fig. 2 Velocity profiles for various bundle lengths
- Fig. 3 Velocity profiles for various locations of the tube bundle

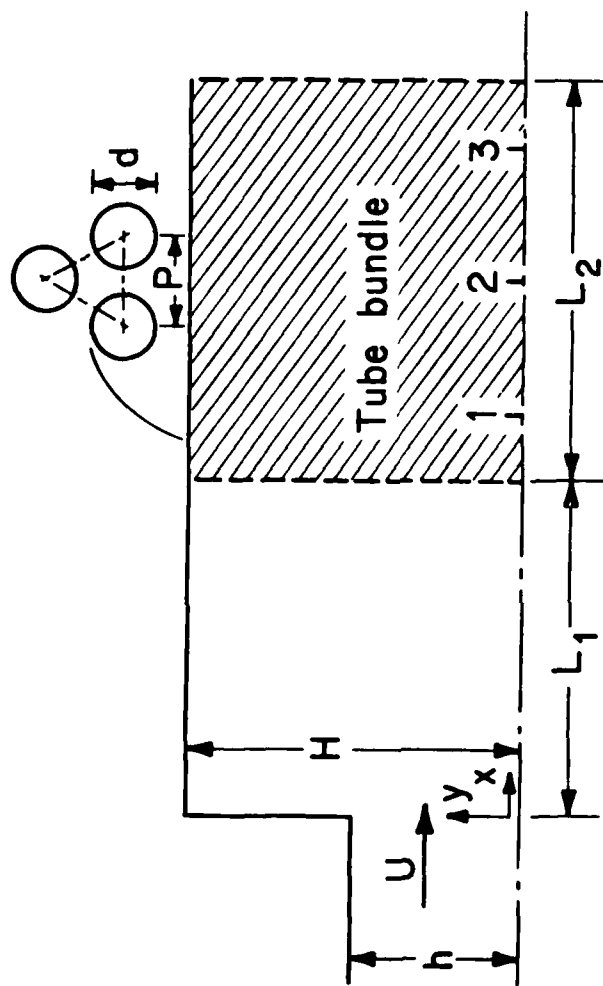


Fig. 1

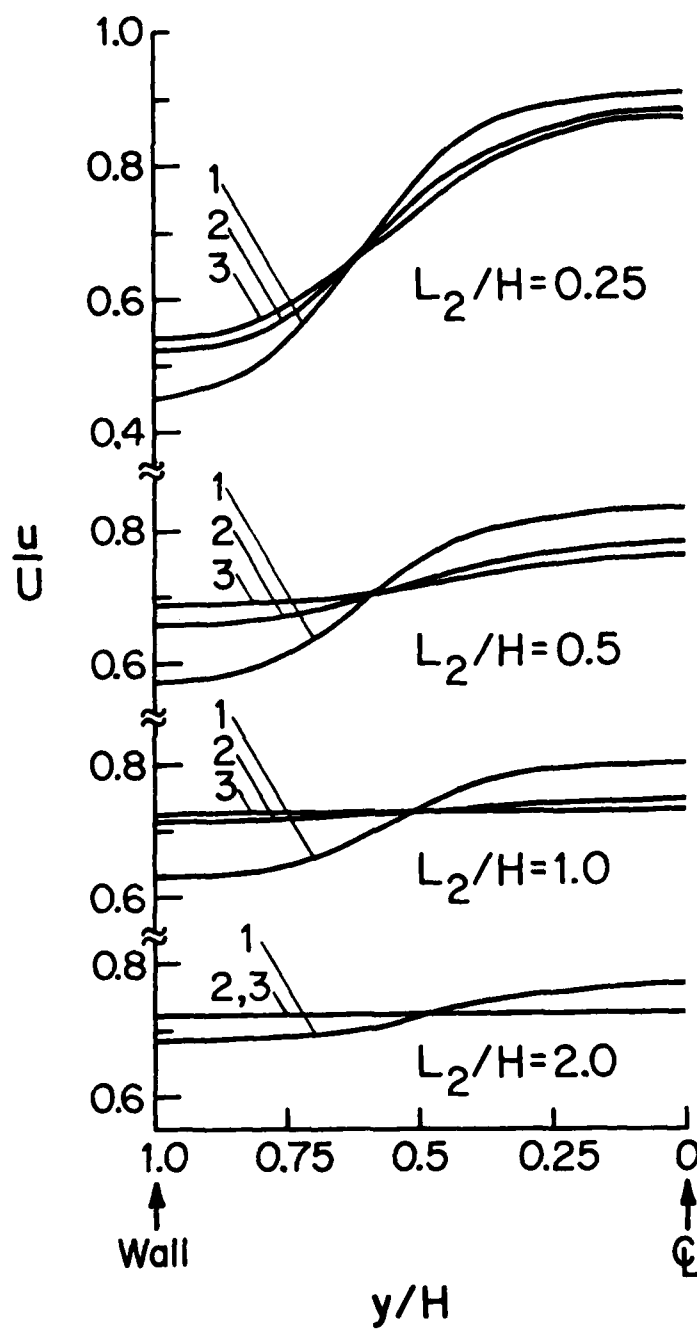


Fig. 2

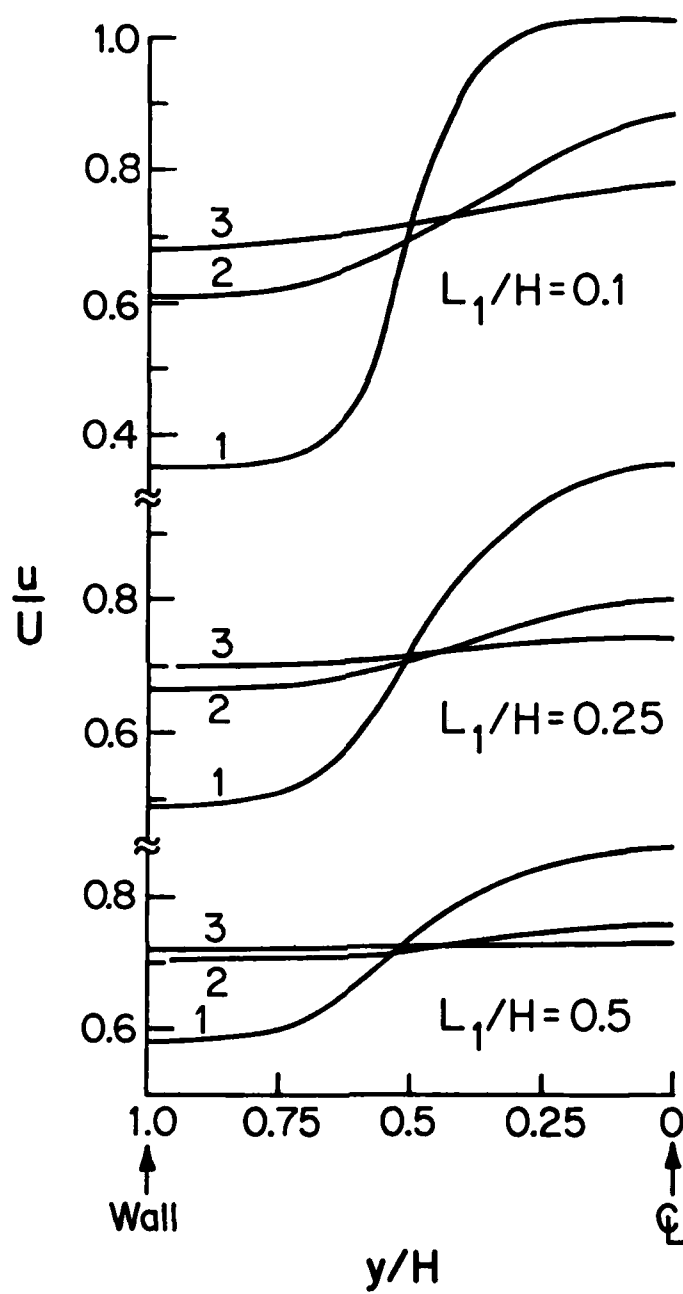


Fig. 3

DISTRIBUTION LIST

HEAT TRANSFER

One copy except
as noted

Mr. M. Keith Ellingsworth
Power Program
Office of Naval Research
800 N. Quincy Street
Arlington, VA 22203

5

Defense Documentation Center
Building 5, Cameron Station
Alexandria, VA 22314

12

Technical Information Division
Naval Research Laboratory
4555 Overlook Avenue SW
Washington, DC 20375

6

Professor Paul Marto
Department of Mechanical Engineering
US Naval Post Graduate School
Monterey, CA 93940

Professor Bruce Rankin
Naval Systems Engineering
US Naval Academy
Annapolis, MD 21402

Office of Naval Research Eastern/
Central Regional Office
Bldg 114, Section D
666 Summer Street
Boston, Massachusetts 02210

Office of Naval Research Branch Office
536 South Clark Street
Chicago, Ill. 60605

Office of Naval Research
Western Regional Office
1030 East Green Street
Pasadena, CA 91106

Mr. Charles Miller, Code 05R13
Crystal Plaza #6
Naval Sea Systems Command
Washington, DC 20362

Heat Exchanger Branch, Code 5223
National Center #3
Naval Sea Systems Command
Washington, DC 20362

Mr. Ed Ruggiero, NAVSEA 08
National Center #2
Washington, DC 20362

Dr. Earl Quandt Jr., Code 272
David Taylor Ship R&D Center
Annapolis, MD 21402

Mr. Wayne Adamson, Code 2722
David Taylor Ship R&D Center
Annapolis, MD 21402

Dr. Win Aung
Heat Transfer Program
National Science Foundation
Washington, DC 20550

Mr. Michael Perlsweig
Department of Energy
Mail Station E-178
Washington, DC 20545

Dr. W.H. Theilbahr
Chief, Energy Conservation Branch
Dept. of Energy, Idaho Operations Office
550 Second Street
Idaho Falls, Idaho 83401

Professor Ephriam M. Sparrow
Department of Mechanical Engineering
University of Minnesota
Minneapolis, Minnesota 55455

Professor J.A.C. Humphrey
Department of Mechanical Engineering
University of California, Berkeley
Berkeley, California 94720

Professor Brian Launder
Thermodynamics and Fluid Mechanics Division
University of Manchester
Institute of Science & Technology
PO88 Sackville Street
Manchester M601QD England

Professor Shi-Chune Yao
Department of Mechanical Engineering
Carnegie-Mellon University
Pittsburgh, PA 15213

Professor Charles B. Watkins
Chairman, Mechanical Engineering Department
Howard University
Washington, DC 20059

Professor Adrian Bejan
Department of Mechanical Engineering
University of Colorado
Boulder, Colorado 80309

Professor Donald M. McEligot
Department of Aerospace and Mechanical Engineering
Engineering Experiment Station
University of Arizona 85721

Professor Paul A. Libby
Department of Applied Mechanics and Engineering Sciences
University of California San Diego
Post Office Box 109
La Jolla, CA 92037

Professor C. Forbes Dewey Jr.
Fluid Mechanics Laboratory
Massachusetts Institute of Technology
Cambridge, Massachusetts 02139

Professor William G. Characklis
Dept. of Civil Engineering and Engineering Mechanics
Montana State University
Bozeman, Montana 59717

Professor Ralph Webb
Department of Mechanical Engineering
Pennsylvania State University
208 Mechanical Engineering Bldg.
University Park, PA 16802

Professor Warren Rohsenow
Mechanical Engineering Department
Massachusetts Institute of Technology
77 Massachusetts Avenue
Cambridge, Massachusetts 02139

Professor A. Louis London
Mechanical Engineering Department
Bldg. 500, Room 501B
Stanford University
Stanford, CA 94305

Professor James G. Knudsen
Associate Dean, School of Engineering
Oregon State University
219 Coveall Hall
Corvallis, Oregon 97331

Professor Arthur E. Bergles
Mechanical Engineering Department
Iowa State University
Ames, Iowa 50011

Professor Kenneth J. Bell
School of Chemical Engineering
Oklahoma State University
Stillwater, Oklahoma 74074

Dr. James Lorenz
Component Technology Division
Argonne National Laboratory
9700 South Cass Avenue
Argonne, Illinois 60439

Dr. David M. Eissenberg
Oak Ridge National Laboratory
P.O. Box Y, Bldg. 9204-1, MS-0
Oak Ridge, Tennessee 37830

Dr. Jerry Taborak
Technical Director
Heat Transfer Research Institute
1000 South Fremont Avenue
Alhambra, CA 91802

Dr. Simion Kuo
Chief, Energy Systems
Energy Research Laboratory
United Technology Research Center
East Hartford, Connecticut 06108

Mr. Jack Yampolsky
General Atomic Company
P.O. Box 81608
San Diego, CA 92138

Mr. Ted Carnavos
Noranda Metal Industries, Inc.
Prospect Drive
Newtown, Connecticut 06470

Dr. Ramesh K. Shah
Harrison Radiator Division
General Motors Corporation
Lockport, New York 14094

Dr. Ravi K. Sakhuja
Manager, Advanced Programs
Thermo Electron Corporation
101 First Avenue
Waltham, Massachusetts 02154

Mr. Doug Marron
Engine R&D Branch, Code 5231
NC #4
Naval Sea Systems Command
Washington, D.C. 20362
(Tel 202-692-6874)

Mr. Richard S. Carlton
Director, Engines Division, Code 523
NC #4
Naval Sea Systems Command
Washington, D.C. 20362
(Tel. 202-692-6868)

Mr. Richard F. Wyvill
Engine Design Branch, Code 5232
NC #4
Naval Sea Systems Command
Washington, D.C. 20362
(Tel 202-692-6931)

Mr. Walter Ritz
Code 033C
Naval Ships Systems Engineering Station
Philadelphia, Pennsylvania 19112
(Tel. 215-755-3841)

Dr. Simion Kuo
United Tech. Res. Center
Silver Lane
East Hartford, Conn. 06108
(Tel. 203-727-7258)

Mr. T.M. Herder
Bldg. 464-G2
General Electric Co.
1100 Western Ave.
Lynn, Massachusetts 01910
(Tel. 617-594-3360)

Mr. Ed Strain
AiResearch of Arizona
Dept. 76, Mail Stop 301-2
P.O. Box 5217
Phoenix, Arizona 85010
(Tel 602-267-2797)

Mr. Norm McIntire
Solar Turbines International
2200 Pacific Hwy.
San Diego, CA 92101
(Tel. 714-238-6527)

Mr. Robert W. Perkins
Turbotec Products, Inc.
533 Downey Drive
New Britain, Connecticut 06051

Dr. Keith E. Starner
York Division, Borg-Warner Corp.
P.O. Box 1592
York, PA 17405

Mr. Peter Wishart
C-E Power Systems
Combustion Engineering, Inc.
Windsor, Connecticut 06095

Mr. Henry W. Braum
Manager, Condenser Engineering Department
Delaval
Front Street
Florence, New Jersey 08518

Dr. Thomas Rabas
Steam Turbine-Generator Technical Operations Division
Westinghouse Electric Corporation
Lester Branch
P.O. Box 9175 N2
Philadelphia, PA 19113